Article ID: 1006-8775(2023) 02-0216-20

Thermodynamics and Microphysical Characteristics of an Extreme Rainfall Event Under the Influence of a Low-level Jet over the South China Coast

XU Bi-yu (徐碧裕)[1], LI Hui-qi (黎慧琦)[2, 3], YE Lang-ming (叶朗明)[1], LIU Xian-tong (刘显通)[2, 3]
RAO Xiao-na (饶晓娜)[2], XIAO Hui (肖 辉)[2], XU Jia-min (徐加民)[4], LIN Qing (林 青)[5]
PU Yi-liang (蒲义良)[1], HUANG Qing-lan (黄青兰)[1]
(1. Jiangmen Meteorological Bureau, Jiangmen, Guangdong 529030 China;
2. Guangzhou Institute of Tropical and Marine Meteorology, China Meteorological Administration, Guangzhou 510641 China;
3. China Meteorological Administration Tornado Key Laboratory, Guangzhou 510641 China;
4. Xinhui Meteorological Bureau, Jiangmen, Guangdong 529100 China;
5. Guangdong Meteorological Bureau, Guangzhou 510080 China)

Abstract: In this paper, the data of Automatic Weather Stations (AWSs), ERA5 reanalysis, sounding, wind profile radar, and dual-polarization radar are used to study an extreme rainfall event in the south China Coast on 11 to 12 May 2022 from the aspects of thermodynamics and microphysical characteristics under the influence of low-level jets (LLJs). Results show that: (1) The extreme rainfall event can be divided into two stages: the first stage (S1) from 0000 to 0600 LST on May 12 and the second stage (S2) from 0700 to 1700 LST on the same day. During S1, the rainfall is mainly caused by the upper-level shortwave trough and the boundary layer jet (BLJ), characterized by strong upward motion on the windward side of mountains. In S2, the combined influence of the BLJ and synoptic-system-related low-level jet (SLLJ) increases the vertical wind shear and vertical vorticity, strengthening the rainstorm. In combination with the effect of topography, a warm and humid southwest flow continuously transports water vapor to farther north, resulting in a significant increase in rainfall over the study area (on the terrain's windward slope). From S1 to S2, the altitude of a divergence center in the upper air decreases obviously. (2) The rainfalls in the two stages are both associated with the mesoscale convergence line (MCL) on the surface, and the wind field from the mesoscale outflow boundary (MOB) in S1 is in the same direction as the environmental winds. Due to a small area of convergence that is left behind the MOB, convection moves eastward quickly and causes a short duration of heavy rainfall. In S2, the convergence along the MOB is enhanced, which strengthens the rainfall and leads to strong outflows, further enhancing the surface convergence near the MOB and forming a positive feedback mechanism. It results in a slow motion of convection and a long duration of heavy rainfall. (3) In terms of microphysics, the center of a strong echo in S1 is higher than in S2. The warm-rain process of the oceanic type characterizes both stages, but the convective intensity in S2 is significantly stronger than that in S1, featuring bigger drop sizes and lower concentrations. It is mainly due to the strengthening of LLJs, which makes small cloud droplets lift to melting levels, enhancing the ice phase process (riming process), producing large amounts of graupel particles and enhancing the melting and collision processes as they fall, resulting in the increase of liquid water content (LWC) and the formation of large raindrops near the surface.

Key words: low-level jet; thermodynamics; microphysics; heavy rain; south China coast
CLC number: P443 **Document code:** A
Citation: XU Bi-yu, LI Hui-qi, YE Lang-ming, et al. Thermodynamics and Microphysical Characteristics of an Extreme Rainfall Event under the Influence of a Low-level Jet over the South China Coast [J]. Journal of Tropical Meteorology, 2023, 29(2): 216-235, https://doi.org/10.46267/j.1006-8775.2023.017

1 INTRODUCTION

South China is located in the East Asian monsoon climate zone, and heavy rainfall frequently occurs during the pre-summer rainy season (April to June) due to the influence of warm and humid air from the ocean (Ding [1]; Ding and Chan [2]; Lau et al. [3]). The total precipitation during the pre-summer rainy season in south China accounts for about half of the annual precipitation (Luo et al. [4]), and most of the rainfall is convective rainfall (Luo et al. [5]; Xia et al. [6]). The heavy rainfall during the pre-summer rainy season in south China can be generally divided into two categories: frontal heavy rainfall and warm-sector heavy rainfall. The formation mechanisms for these two categories of heavy rainfall are quite different (Luo et al. [4]; Huang [7]; Zhao et al. [8]; Luo [9]; Du and Chen [10]). Frontal heavy rain occurs near synoptic-scale cold fronts formed by the convergence of northerly cold and dry air and southerly warm and moist air (Ding [1]; Zhao et al. [8]). The warm sector heavy rain mostly occurs in the

Received 2022-10-06; **Revised** 2023-02-15; **Accepted** 2023-05-15
Funding: National Natural Science Foundation of China (U2242203, 41975138, 42275008); Natural Science Foundation of Guangdong Province (2019A1515010814, 2021A1515011415); Science and Technology Development Fund Project of Guangdong Meteorological Bureau (GRMC2020M27); Jiangmen Young science and technology talents lifting Project (2022-2023)
Biography: XU Bi-yu, Intermediate Engineer, primarily undertaking research on short-term weather forecasting.
Corresponding author: YE Lang-ming, email: yelm@gd121.cn

warm area, 200 km ahead of the front, under weakly synoptic forcing (Huang [7]; Lin et al. [11]). Both categories of heavy rainfall can lead to serious economic damage and loss of life.

The formation of a rainstorm in the pre-summer rainy season in south China is closely related to LLJs (Chen et al. [12]; Chen et al. [13−14]; He et al. [15]), topography (Xia and Zhao [16]; Li et al. [17]; Wang et al. [18]; Rao et al. [19]), land-sea contrast (Wu et al. [20]; Li et al. [21]), mesoscale convergence line (MCL) (Chen [22]; Xu et al. [23]; Wu and Luo [24]; Liu et al. [25]), and cold pool (Liu et al. [25]; Wang et al. [26]). Among them, the LLJs always play an important role. There are many kinds of research focused on LLJs through climatological statistics, meteorological observation, and numerical simulation in China in recent years (He et al. [15]; Du et al. [27−30]; Zhang et al. [31]; Li et al. [32]; Shu et al. [33]; Miao et al. [34]). LLJs appear in many parts of the world (Stensrud [35]; Rife et al. [36]), which are generally referred to as a strong wind speed band within a few kilometers of the near-surface layer in the atmosphere. According to different heights of the maximum wind speed zone and the influence of the weather system, the LLJs can be further subdivided into two types: the first is named BLJ, which occurs below 1 km and is always related to the boundary layer process; The second is SLLJ that occurs above the BLJ and has a larger vertical range (~1−4 km), which is more closely related to synoptic systems (Du et al. [27−28]; Chen et al. [37]). These two types of LLJs have different formation processes and characteristics. The BLJ is mainly formed by Blackadar inertial oscillation mechanism (Blackadar [38]) and forcing from the Holton baroclinic topography mechanism (Holton [39]) or the combination of them (Du and Rotunno [40]; Shapiro et al. [41]). It is also affected by large-scale circulations, synoptic systems, or sub-synoptic systems, and usually happens in coastal areas or near highlands (Du and Chen [10]). The SLLJ is usually formed by weather disturbance (Du et al. [30]; Chen and Yu [42]; Tao and Chen [43]; Xue et al. [44]). Numerous studies have shown that the transport of warm and moist air by the LLJs provides favorable thermal conditions and causes convergence at the end of the jet (Astling et al. [45]; Trier and Parsons [46]; Higgins et al. [47]; Trier et al. [48]; Chen et al. [49]). The vertical coupling of the BLJ and SLLJ from the lower tropospheric may have profound impact on the development of heavy rainfall storms through thermodynamic and kinematic factors (Du and Chen [50]). Du and Chen [10] have found that the BLJ and SLLJ are closely related to the heavy rainfall in the warm sector and frontal system, respectively, and the double LLJs in the humid southwest flow play an important role during the heavy rainfall in south China. The frontal heavy rainfall is closely related to the SLLJ, with the maximum wind speed occurring at 850−700 hPa. The stronger the cold front, the stronger the southwest wind on the south side of the front, which is conducive to strengthening rainfall near the front. However, the heavy rainfall in the warm sector several hundred kilometers away from the front is closely related to the BLJ at 925 hPa, which usually appears in the northern part of the South China Sea, and of which the maximum wind speed appears in the early morning. The variation of the BLJ is mainly caused by the shortwave trough at high altitudes.

The dynamic and thermodynamic differences caused by the LLJs may lead to differences in microphysical characteristics, ultimately leading to changes in surface precipitation. However, due to the limitation of previous observations in south China, the microphysical differences in precipitation under the influence of different LLJs still need to be clarified. Dual-polarization radars have become one of the most important tools for studying cloud microphysics (Bringi et al. [51]; Kumjian and Ryzhkov [52]). They provide additional information such as the shape, size, and orientation of particles (Bringi and Chandrasekar [53]; Zrnic and Ryzhkov [54]), which are widely used in the research on various types of storms all around the world (Barnes and Houze [55]; Chen et al. [56]; Lang et al. [57]; Matsui et al. [58]; Rowe et al. [59−60]; Wen et al. [61]; Pu et al. [62]).

An extreme rainfall event occurred in the coastal areas of south China from 11 to 12 May 2022, with the maximum rainfall of 24 hrs reaching 561.7 mm at Chixi Station in Taishan, Jiangmen City. The dynamic, thermodynamic, and microphysical characteristics of precipitation in two stages under different backgrounds of LLJs effects are compared and analyzed in this paper. The primary purpose of this study is twofold: firstly, to investigate the mechanism of LLJs, including the BLJ and SLLJ, in triggering and maintaining heavy rainfall; secondly, to investigate the difference in microphysical characteristics in rainstorm evolution before and during the influence of LLJs.

The remainder of this study is organized as follows. The data and methods are introduced in the following section. Section 3 describes the evolution of rainfall and convection. The synoptic background and the environmental conditions are presented in section 4. The development of mesoscale surface conditions is discussed in section 5, and the microphysical characteristics of the rainstorm are shown in section 6. The conclusion is presented in the final section.

2 DATA AND METHODS

2.1 *Data and instruments*

Synoptic situations and thermodynamic characteristics are analyzed by using ERA5 reanalysis data with the spatial resolution of 0.25 °×0.25 ° and 1 h time interval (https://cds.climate.copernicus.eu/cdsapp#!/home) provided by the European Centre for Medium-Range Weather Forecasts (ECMWF). Sounding data from Yangjiang and Hong Kong stations are used to

analyze mesoscale environmental conditions (Fig. 1a, in triangle). Wind, precipitation, and temperature data at hourly intervals from automatic weather stations (AWSs) are used for rain and surface mesoscale analyses. Wind profile radars in Hailing Island and Zhuhai are used to analyze the coupling process of BLJ and SLLJ in the key region (Fig. 1a, in green diamond). The microphysical characteristics of precipitation are analyzed based on the observation of an S-band dual-polarization radar data, the retrieval variables, e. g., contents of liquid water and ice water, and the hydrometeor classification retrieved by a Guangzhou radar and a Zhuhai radar. The radar adopts the VCP21 scanning mode, and the radial resolution is 0.25 km. The quality control of ground clutter and biological scattering is carried out by using the methods of Chen et al. [49] and Li et al. [63]. Lightning data detected by EN lightning positioning system is used to compare and analyze the intensity of convection in the two stages.

2.2 *Methods*

2.2.1 CALCULATION OF MOIST POTENTIAL VORTICITY

Wu et al. [64] proposed that the moist potential vorticity (MPV) in the *p*-coordinate system is conserved, which could be decomposed into the barotropic term (vertical component, MPV1) and baroclinic term (horizontal component, MPV2) under the assumptions that the horizontal variation of atmospheric vertical velocity is much less than the vertical shear of horizontal velocity and satisfies hydrostatic approximation. The expressions are as follows:

$$\mathrm{MPV} = \mathrm{MPV1} + \mathrm{MPV2} \tag{1}$$

$$\mathrm{MPV1} = -g\left[f + \left(\frac{\partial v}{\partial x} - \frac{\partial u}{\partial y} \right) \right] \frac{\partial \theta_e}{\partial p} \tag{2}$$

$$\mathrm{MPV2} = g\left(\frac{\partial v}{\partial p} \cdot \frac{\partial \theta_e}{\partial x} - \frac{\partial u}{\partial p} \cdot \frac{\partial \theta_e}{\partial y} \right) \tag{3}$$

In the above equations, f is the geostrophic vorticity and θ_e is the equivalent potential temperature. MPV1 depends on the vertical component of absolute vorticity and convective stability ($\partial\theta_e / \partial p$), while MPV2 depends on vertical wind shear and horizontal gradient of equivalent potential temperature. The strengthening LLJs will increase the vertical wind shear. According to the MPV principle and slantwise vorticity development theory (Hoskins [65–66]), due to the increased gliding along moist isentropic surfaces (negative MPV2), the vertical wind shear and the increase in moist baroclinity are conducive to the development of vertical vorticity and the maintenance of rainstorms (Meng et al. [67]).

2.2.2 CALCULATION OF LIQUID AND ICE WATER CONTENTS, AND RETRIEVAL OF RAINDROP SIZE DISTRIBUTION

Based on the polarization variables detected by dual-polarization radar, the phase states of the particles can be identified and classified (Park et al. [68]). In this paper, the optimized hydrometeor classification algorithm (HCA) proposed by Wu et al. [69] was used to classify radar echoes into the following 10 categories: ground clutter or anomalous propagation (GC / AP), biological scatter (BS), dry aggregated snow (DS), wet snow (WS), crystals of various orientations (CR), graupel (GR), big drops (BD), light and moderate rain (RA), heavy rain (HR), and a mixture of rain and hail (RH). From the particle types, microphysical processes can be inferred. For example, DS represents aggregation, WS implies melting, and GR is related to riming.

The liquid and ice water contents can be calculated from the dual-polarization radar. In this paper, the constrained particle size distribution method proposed by Zhang et al. [70] was used to retrieve the liquid water content in pure rain. For rain in the mixed phase of ice water, the differential reflectivity (Z_{DP}, units: dB) method proposed by Golestani et al. [71] was used to estimate the horizontal polarization reflectivity (Z_{H}) of rain and ice (Z_{ice}). The Z_{rain}-Z_{DP} relationship shown as follows was obtained from two years of raindrop spectrum observation data in Guangdong province:

$$Z_{\mathrm{rain}} = 0.0044 \times Z_{\mathrm{DP}}{}^{2} + 0.58054 \times Z_{\mathrm{DP}} + 16.591 \tag{4}$$

$$Z_{\mathrm{ice}} = Z_{\mathrm{H}} - Z_{\mathrm{rain}} \tag{5}$$

The *Z-M* relationship of previous studies (Cifelli et al. [72]; Wang and Carey [73]; Chang et al. [74]; Carey and Rutledge [75]; Wang et al. [76]; Wu et al. [77]) was used to calculate the liquid water content and ice water content:

$$\mathrm{LWC} = 3.44 \times 10^{-3} \left(Z_{\mathrm{rain}} \right)^{4/7} \tag{6}$$

$$\mathrm{IWC} = 1000\pi\rho_i N_0^{\frac{3}{7}} \left(\frac{5.28 \times 10^{-18} Z_{\mathrm{ice}}}{720} \right)^{4/7}, \tag{7}$$

where ρ_{i} is the ice density, and N_0 is the intercept index, assuming the ice follows an inverse exponential distribution. Eq. (7) was used to calculate the ice water content for pure ice.

The three-parameter Γ function can well reflect the characteristics of raindrop spectrum distribution (DSD), and its scale distribution function can be expressed as:

$$N(D) = N_0 D^{\mu} \exp(-\Lambda D), \tag{8}$$

where N_0 (units: $\mathrm{mm}^{-1-\mu}\ \mathrm{m}^{-3}$) is the intercept, μ is the shape factor, and Λ (mm^{-1}) is the slope. The curve is sunken or raised when $\mu > 0$ or $\mu < 0$, respectively. When μ=0, it is the M-P (Marshall and Palmer [78]) exponential distribution. When DSD is given $N(D)$, the radar reflectivity (Z, units: dBZ), rainfall rate (R, units: mm h^{-1}), rainwater content (W, units: g m^{-3}), and total raindrop concentration (N_t, units: m^{-3}), Z_{HH} and Z_{DR} detected by the dual-polarization radar can well characterize DSD changes and estimate the precipitation. The relation between Z_{HH} and $N(D)$:

$$Z_{\mathrm{HH}} = \frac{4\lambda^4}{\pi^4 |K_{\mathrm{W}}|^2} \int_{D_{\min}}^{D_{\max}} |f_{\mathrm{HH}}(D)|^2 N(D)\, \mathrm{d}D, \tag{9}$$

where λ is the radar wavelength, K_{W} is the permittivity of water, and f_{HH} (D) is the back-scatter amplitude of the raindrop when it is horizontally or vertically polarized. Z_{DR} is the ratio of radar reflectance factor in the

horizontal direction and vertical direction, expressed as:

$$Z_{DR} = 10 \times \lg\left(\frac{Z_{HH}}{Z_{VV}}\right) \quad (10)$$

A data filtering method (R>5 mm h^{-1}, Nt >1000) proposed by Zhang et al. [79] was used to reduce the error caused by sampling influence in 6966 2DVD observed samples from May to August 2016 in south China. The μ-Λ relationship is obtained by polynomial least squares fitting:

$$\Lambda = 0.024\mu^2 + 0.867\mu + 2.453 \quad (11)$$

A constrained gamma (C-G) model proposed by Liu et al. [25] for the retrieval of raindrop size distributions (DSDs) algorithm was adopted in this paper. The specific fitting formula is as follows:

$$\Lambda = 2.111 \times Z_{DR}^{-1.044} \quad (12)$$

$$N_0 = Z_{HH} \times 10^{-0.00188\Lambda^4 + 0.0447\Lambda^3 - 0.372\Lambda^2 + 1.898\Lambda - 3.065} \quad (13)$$

After verification by Pu et al. [62], the raindrop spectrum data retrieved by this scheme is consistent with the results of the 2DVD observation.

3 OVERVIEW OF THE HEAVY RAINFALL

From 10 to 13 May 2022, Guangdong experienced heavy rainfall for four consecutive days. It was also the strongest rainstorm in May in the past two decades. This paper focuses on the rainfall process from 2000 LST 11 May to 2000 LST 12 May, during which the heaviest rainfall occurred (Fig. 1b). Heavy rainfall (greater than

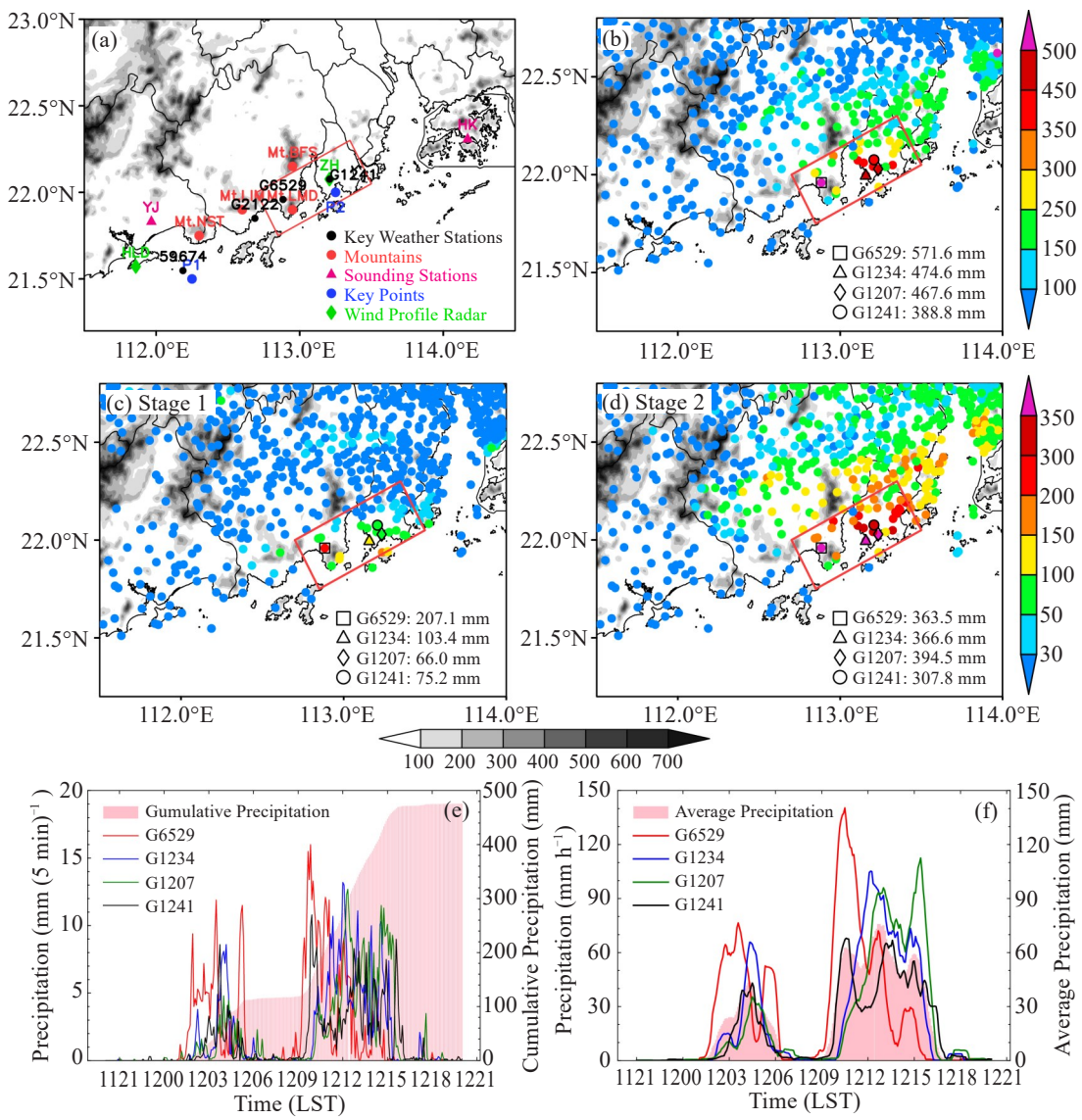

Figure 1. (a) Key weather stations (black dot) mentioned in the text, mountains (red dot), sounding stations (pink triangle), key points (blue dot), wind profile radar (green diamond) and terrain height in south China (shaded, units: m); (b) Accumulated precipitation from 2000 LST 11 May to 2000 LST 12 May 2022 observed by the AWSs; (c) Accumulated precipitation in S1 (from 0000 to 0600 LST12 May 2022); (d) Accumulated precipitation in S2 (from 0700 to 1700 LST 12 May 2022) (units: mm); red box represents study area; black box, triangle, diamond and circle represent the position of stations G6529, G1234, G1207 and G1241, respectively; (e) Time series of cumulative precipitation in every 5 minutes (line, unit: mm (5 min)$^{-1}$) and the average cumulative precipitation of the four stations (shaded, units: mm); (f) Time series of cumulative precipitation in every 60 minutes (line; units: mm h^{-1}) and the average precipitation of 4 stations (shaded, units: mm h^{-1}) (the red, blue, green and black lines represent stations G6529, G1234, G1207 and G1241, respectively).

100 mm) was mainly located on the south side of Beifeng Mountain (Mt. BFS in Fig. 1a) and near the windward slope of Mountain Liangmaoding in Chixi, Taishan (Mt. LMD in Fig. 1a) (i.e., the study area, red box in Fig. 1a). Three AWSs recorded more than 400 mm of accumulated precipitation, of which station G6529 recorded a maximum of 571.6 mm in 24 hrs (Fig. 1b), and the maximum hourly rainfall reached 140.3 mm (from 0930 to 1030 LST 12 May) (Fig. 1f). The rainfall in the study area was mainly divided into two stages, namely from 0000 to 0600 and from 0700 to 1700 LST 12 May, respectively. The rainfall in S2 was significantly greater than in S1, and the maximum accumulated precipitation of the corresponding station was 207.1 mm and 363.5 mm respectively (Fig. 1c, 1d). At 2300 LST 11 May, convective cells were initiated and developed between the Hailing Island of Yangjiang and the Naqin Peninsula of Taishan (Fig. 1a, between HLD and Mt. NST, and Fig. 2a). About one hour later, convective cells were significantly enhanced along the Taishan coast (with radar reflectivity exceeding 35 dBZ) (Fig. 2b), and then rapidly moved eastward along the coastline to affect the study areas, which led to the heavy rainfall in the study area during 0000 and 0600 LST 12 May (S1). Rainfall in the study areas reached a peak during 0200 and 0400 LST 12 May within S1; the maximum accumulated precipitation reached 76.5 mm in 60 min (from 0235 to 0335 LST 12 May) (Fig. 1f, G6529) and the 5-minute rainfall reached the maximum of 11.9 mm (from 0325 to 0330 LST 12 May) (Fig. 1e). At 0600 LST 12 May, after the heavy rainfall of S1, the initial convection was triggered again extensively in range to farther north in contrast to S1 (Fig. 2d). At 0700 LST 12 May, two mesoscale convective systems (MCSs) appeared upstream and downstream of the place where the convection was triggered, and gradually approached each other from 0800 to 0830 LST 12 May. At about 0900 LST 12, the two MCSs merged and strengthened not far away from the upstream of the study area, and gradually formed a convective belt from southwest to northeast affecting the study area (Fig. 2e-2h). From 1000 to 1400 LST 12 May, new convective cells merged with the previous convective cells, which led to the echo training in the study area. The radar reflectivity was maintained at a high level (Z_H >50 dBZ) over the study area (Fig. 2i-2k), resulting in rainfall exceeding 10 mm $(5\ min)^{-1}$ for about 50 minutes (from 0935 to 1025 LST) in S2, with the maximum at 16 mm $(5\ min)^{-1}$ (from 0945 to 0950 LST) (Fig. 1e). Subsequently, at about 1600 and 1700 LST, the heavy rainfall belt gradually moved eastward out of the study area, and the convective intensity was greatly weakened, followed by the rain intensity (Fig. 2l).

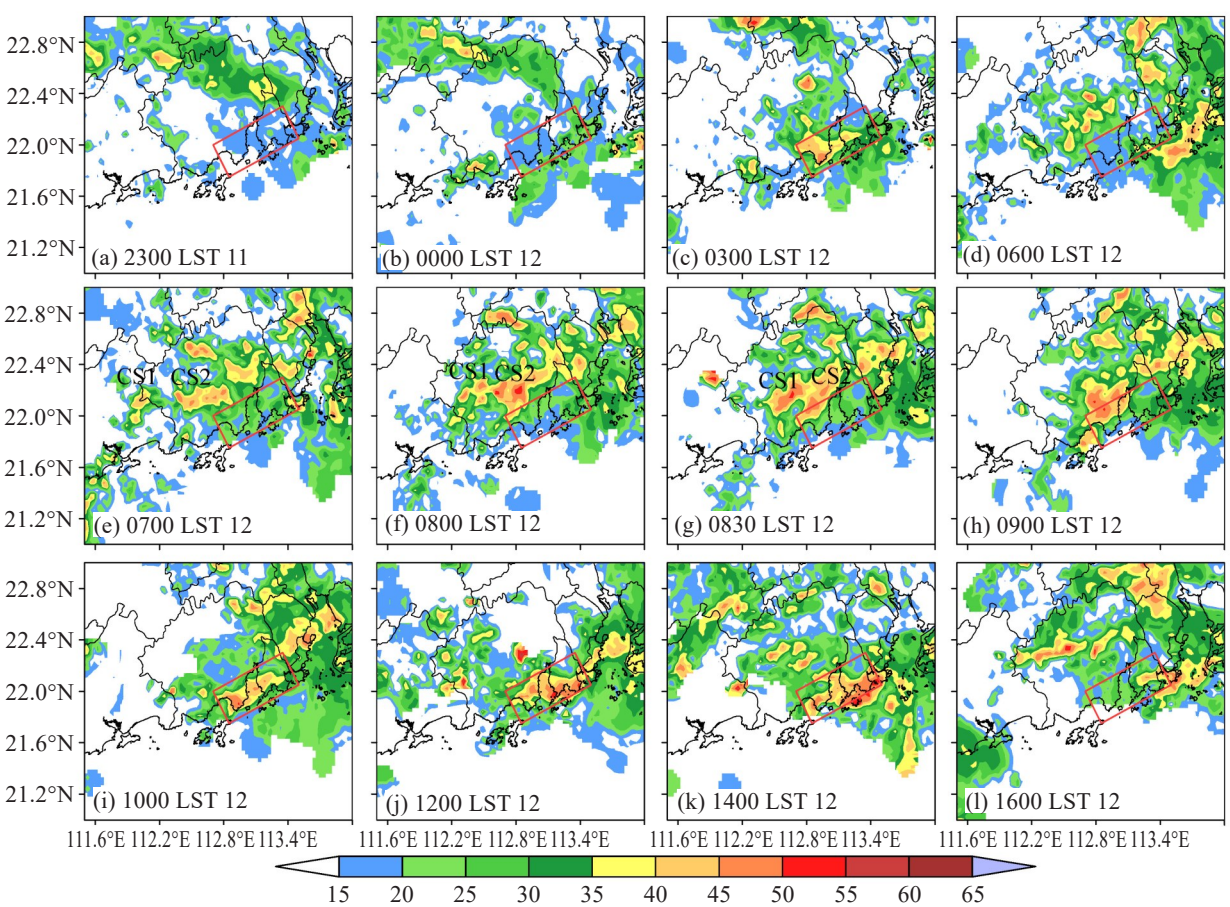

Figure 2. CAPPI of the Z_H (units: dBZ) at 2 km above sea level from Guangzhou dual-polarization radar. The red box represents the study area. CS1 and CS2 in (e)-(g) represent two different convective systems.

The analysis above reveals that the two stages of the heavy rainfall event in the study area exhibit significantly different characteristics in terms of rainfall intensity and convection evolution. Therefore, this paper will further examine the distinct features of the two stages of this extreme rainfall event, focusing on the dynamic, thermal, and microphysical structures.

4 EVOLUTION OF THERMAL AND DYNAMIC CHARACTERISTICS

Based on ERA5 reanalysis data, it was observed that during the first period of heavy precipitation (S1), a shortwave trough developed upstream of the study area at 500 hPa and moved southeastward (Fig. 3a). The contour of 5730 geopotential meters (units: gpm) moved southward from the inland area to the coastline (Fig. 3b) within an hour from 0200 to 0300 LST on May 12. The shear lines at 850 hPa and 925 hPa were quasi-stationary or moved slightly southward in the north of the study area (Fig. 3a, 3b, 3e). A jet stream (BLJ) with wind speed greater than 10 m s^{-1} appeared at 925 hPa in the southern part of the study area, while an SLLJ also appeared at 850 hPa, and the center of the two jet streams overlapped (Fig. 3b, 3e). At the same time, the horizontal wind speed convergence zone along the coastline appeared in the study area (not shown), and the high pseudo-equivalent potential temperature area (>350 K) was elevated to 850 hPa under the force of coastal topography (Fig. 4a). Additionally, the convective precipitation enhanced under the influence of the warm advection at the low level of 925 hPa (not shown). In S1, the continuous downward transportation of high-altitude

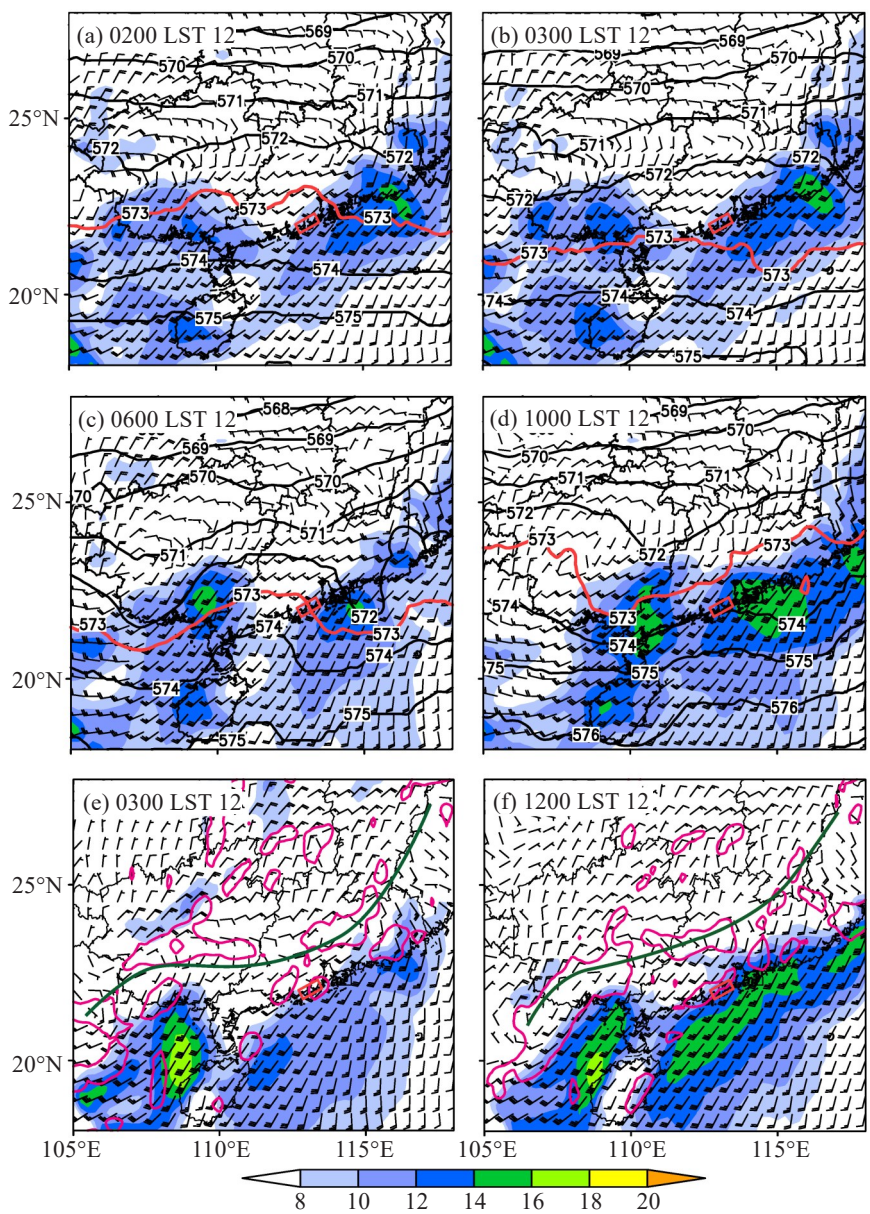

Figure 3. (a)-(d): Geopotential height field at 500 hPa (contour, units: 10 gpm) and wind field at 850 hPa (units: m s^{-1}; full barb represents 4 m s^{-1}; shadings represent wind speed ≥8 m s^{-1}); (e)-(f): Wind field (units: m s^{-1}; full bar represents 4 m s^{-1}; shading is wind speed) and vorticity (contour line represents value ≥0.8×10^{-4} s^{-1}) at 925 hPa.

momentum in the vertical direction provided dynamic support for developing low-altitude systems and was an important condition for generating the LLJs (Wu et al.[80]; Jin et al. [81]; Cao et al.[82]). This may be caused by the downward sliding of a high-value potential vortex. The front end of the strong wind speed area shows a strong upward movement. Therefore, while the southwest jet is expanding downward, there may be momentum transportation, causing the strengthening of low-level disturbance.

At 0600 LST on May 12, a high-pressure ridge extending northward appeared at the level of 500 hPa, and the study area was in front of the ridge, which suppressed precipitation and resulted in intermittent rainfall in the study area (Fig. 3c). With the continuous development of LLJs, a low vortex circulation was produced near Guangxi at 850 hPa and moved southward (Fig. 3c, 3d). Meanwhile, the gradient of geopotential height over the study areas increased, and the wind speed at the levels of BLJ and SLLJ started to strengthen. Under the influence of the LLJs, the positive vorticity center was generated at 925 hPa in the study area due to the strong cyclonic curvature in the left front of the LLJs (Fig. 3e, 3f).

At the beginning of S2 (before 0700 LST 12 May), the jets at both levels of 850 hPa and 925 hPa were strengthened, especially those at 850 hPa. Within the following hours after 1000 LST 12 May, the strong wind speed band at 850 hPa was farther north compared with that at 925 hPa (Fig. 4d), resulting in the study area lying in the exit zone of the BLJ at 925 hPa and the entrance zone of the SLLJ at 850 hPa, so that the coupling of the two jets appeared. The vertical coupling of the two LLJs in S2 was similar to the conceptual model of dual jet streams (LLJs) proposed by Du and Chen [10, 50]. Over the study area, the vertical coupling of boundary layer convergence and higher-level divergence provides uplifting and vapor conditions conducive to the generation and development of convection.

The cross-sections of the pseudo-equivalent potential temperature at 1000 LST 12 (Fig. 4b) show that with the strengthening of the LLJs, the secondary meridional circulation was more likely to be excited above 700 hPa, which became the link between high and low levels of synoptic systems, coupling the BLJ with the SLLJ easily, and continuously transporting water vapor to the farther north region instead of developing to higher altitudes (Fig. 4b). Near the land-sea boundary, the high-value area of the equivalent potential temperature in S2 was closer to the ground, and the wind speed near the surface was greater than that in S1 (Fig. 4a, 4b). Strengthening BLJ and SLLJ transported high energy and water vapor to the coast, increasing precipitation under the influence of local coastal terrain. Therefore, more severe rainfall occurred in front of the windward slope of the terrain at 22 °N (Fig. 1b). It is

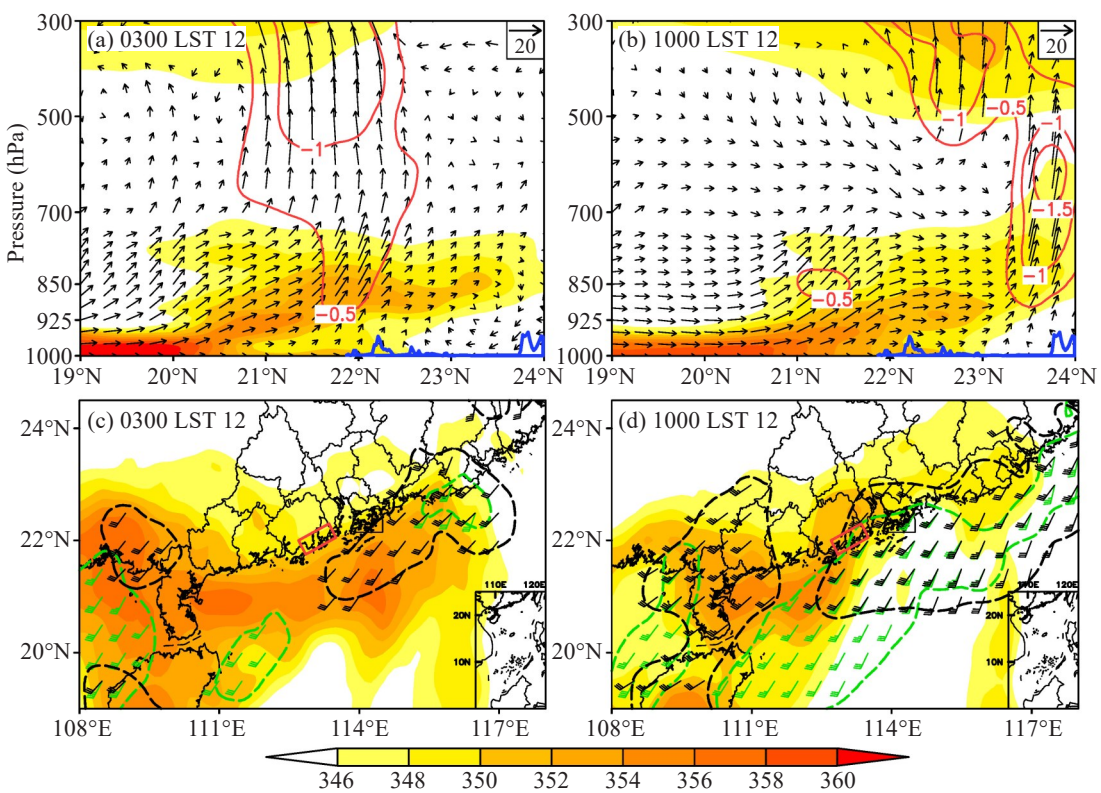

Figure 4. (a)-(b): Cross-sections along 113 °E (solid triangle represents position near G6529; the blue line represents topography altitude) of pseudo-equivalent potential temperature (shaded; units: K), vertical velocity (red contour, units: Pa s^{-1}), and the *v* wind and vertical velocity multiplied by 20; (c)-(d): Horizontal distribution of pseudo-equivalent potential temperature (shaded, units: K), wind field at 850 hPa and 925 hPa (black barb and contours represent wind speed ≥12 m s^{-1} at 850 hPa; green color represents wind speed at 925 hPa).

evident that the warm and moist tongue extended from the coast to the inland in the study area at 1000 LST 12 (Fig. 4d), while it did not stretch inland at S1 (Fig. 4c). It could also be confirmed by the distribution of MPV1 and MPV2 that the rising motion was strong in S1, but mainly in the south of the study area. The absolute values of MPV1 and MPV2 between 975 hPa and 850 hPa in the lower layer were small, indicating that the slope of the isentropic plane in S1 was small, with more stability compared to that in S2 (Fig. 5a). However, after the strengthening of the BLJ and SLLJ in S2, both MPV1 and MPV2 tilted to the north from the lower layer to the upper layer. The extreme range of MPV1 expanded, and the center of MPV2 strengthened, corresponding to each other (Fig. 5b). The MPV2 was related to the slope of the isentropic plane, and its value was related to the vertical wind shear and the moist baroclinicity (i. e., the horizontal gradient of the equivalent potential temperature). Under the MPV conservation, the vertical wind shear or the increase in moist baroclinic could lead to the increase of vertical cyclonic vorticity due to the incline of the isentropic plane. In addition, the more tilted the isentropic plane, the more significantly the vertical cyclonic vorticity grew, maintaining the rainstorm in S2.

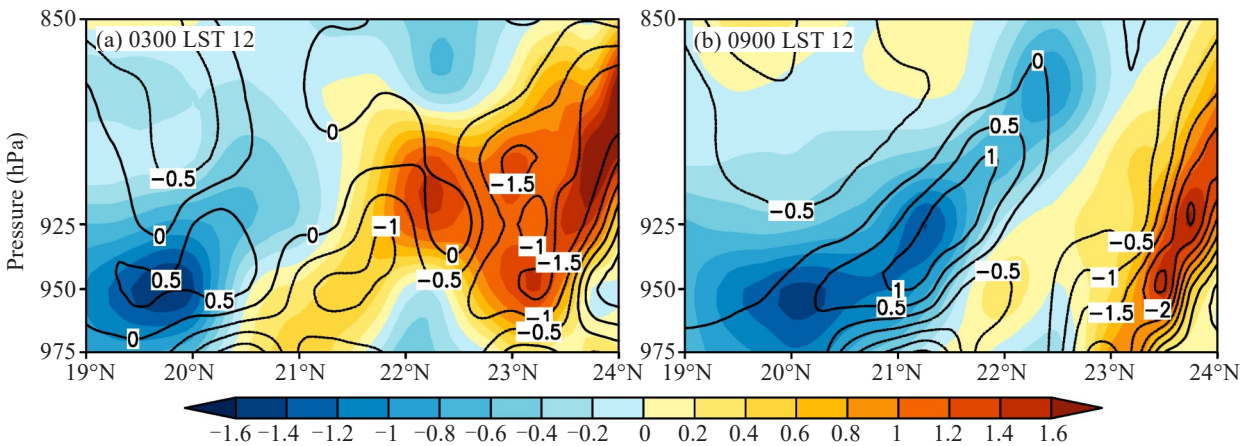

Figure 5. Cross-sections of moist potential vorticity: (a) vertical component (MPV1) (shaded, units: 10^{-6} m^2 s^{-1} K kg^{-1}) and (b) horizontal component (MPV2) (contour, units: 10^{-7} m^2 s^{-1} K kg^{-1}).

From the evolutionary perspective of the vertical circulation (Fig. 6a, 6b), the height of the southwesterly jets decreased from 0200 to 0600 LST 12, leading to the jets occurring at the boundary layer. The vertical wind shear increased and strong warm advection occurred from 925 hPa to 850 hPa during 0600 to 0800 LST 12 May in S2 (Fig. 6a). From S1 to S2 (0000 to 1700 LST 12 May), the positive vorticity center at 500 hPa descended to the lower layer, with the height of its positive center decreasing to 850 hPa at 0500 LST, and continued to decrease and remained at about 925 hPa from 1100 to 1600 LST (Fig. 6b). Synchronously, the height of the upper divergence center decreased from 500 hPa to 700 hPa, and the convergence near the BLJ at 925 hPa enhanced during 0200 and 1000 LST (Fig. 6b). The decreased height of the coupling effect between high and low synoptic systems further indicated the influence of the enhancement of the LLJs, especially the BLJ. This could also be illustrated by the distribution of water vapor fluxes and flux divergence inside and outside the study area (Fig. 6c, 6d). In the study area, the height of the convergence and divergence center of water vapor flux over P2 (as indicated in Fig. 1a) was lower than that at P1 (as indicated in Fig. 1a) outside the study area, and so was the stronger intensity. At P1, the water vapor at the low level was divergent from 0200 to 0500 LST 12 May, while it became convergent more often at P2. In S1, the strong convergence zone of water vapor flux was maintained near 950 hPa in the boundary layer, and the center of water vapor flux appeared near 900 hPa at 0500 LST (the intensity of the center was above 20 g cm s^{-1}) (Fig. 6d). At 1400 LST in S2, the area of the high-value center of water vapor flux expanded, and the height of the high-value center decreased to 950 hPa (the central intensity was above 24 g cm s^{-1}) (Fig. 6d). Additionally, the height of the divergence center of water vapor flux at the upper air near 500 hPa decreased to 800 hPa from 2300 LST 11 to 1100 LST 12 May (Fig. 6d), which coacted with the LLJs and enhanced the coupling between BLJ and SLLJ.

Regarding the atmospheric environment during S1 and S2 of the heavy rainfall, sounding observations at Yangjiang (YJ) and Hong Kong (HK) stations at 2000 LST 11 May were selected for further analysis (Fig. 7a, 7b). The horizontal winds changed from southwesterly to westerly, indicating warm advection below 500 hPa. The 0−3 km vertical wind shear (VWS) was 12.7 m s^{-1} and 9.3 m s^{-1} in YJ and HK, respectively, which favored the formation of multicell-type storms (Markowski and Richardson [83]). The high convective available potential energy (CAPE; 2236 J kg^{-1}), a huge amount of precipitable water (PW; 67 mm), and the deep warm

cloud layer (about 4.8 km) between the lifting condensation level (LCL, 0.178 km above ground level) and the 0 ℃ level (4.9−5.0 km) were conducive to the warm-rain process (Li et al. [63]).

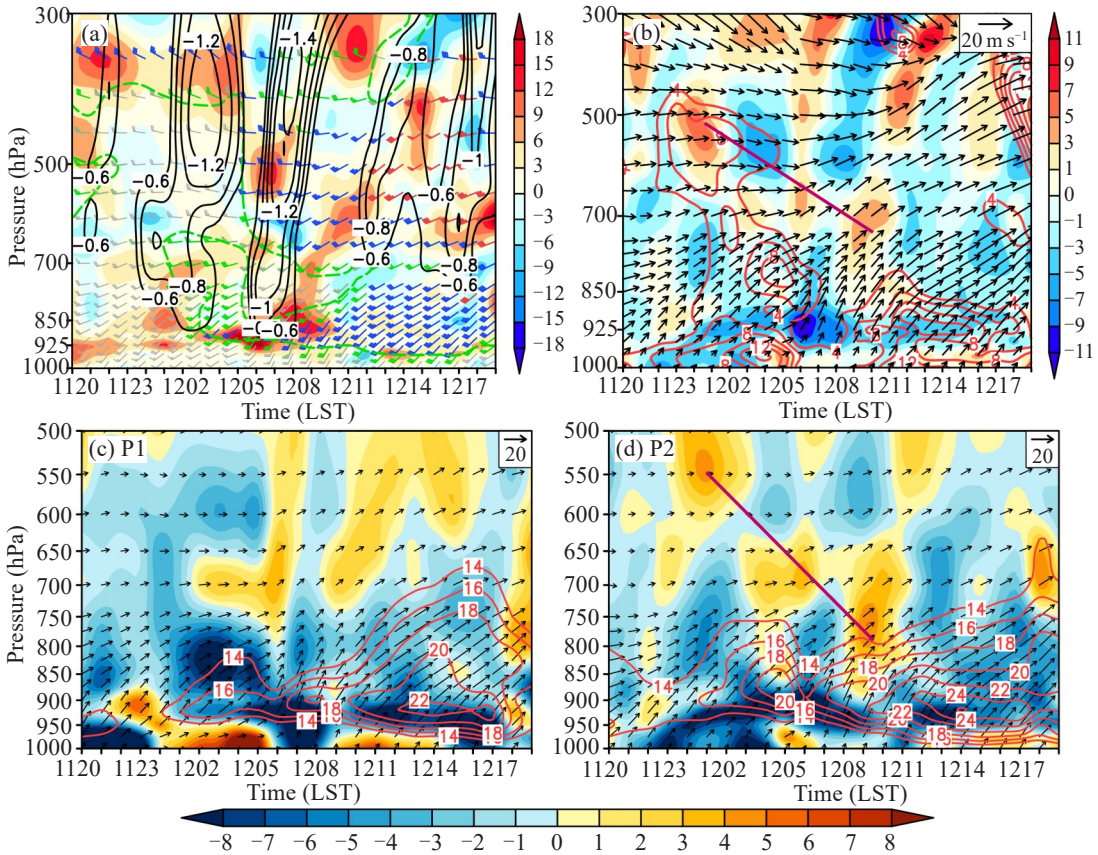

Figure 6. (a) Temporal evolution of the vertical profile of horizontal wind (units: m s^{-1}; full bar represent 4 m s^{-1}; green and green dot contour >10 m s^{-1}; blue >12 m s^{-1}; red >16 m s^{-1}), vertical velocity (black contour, units: Pa s^{-1}), and thermal advection (shaded, units: 10^{-5} K s^{-1}) over station G6529; (b) Vorticity (contour, units: 10^{-5} s^{-1}), divergence (shaded, units: 10^{-5} s^{-1}) and horizontal wind (vector) over station G6529; (c, d) Water vapor flux (red contours, units: g cm s^{-1}) and divergence of moisture flux (shaded, units: g cm^2 s^{-1}) (dark purple line shows the movement of high-level divergence center; the positions of P1 and P2 are marked in blue dots in Fig. 1a).

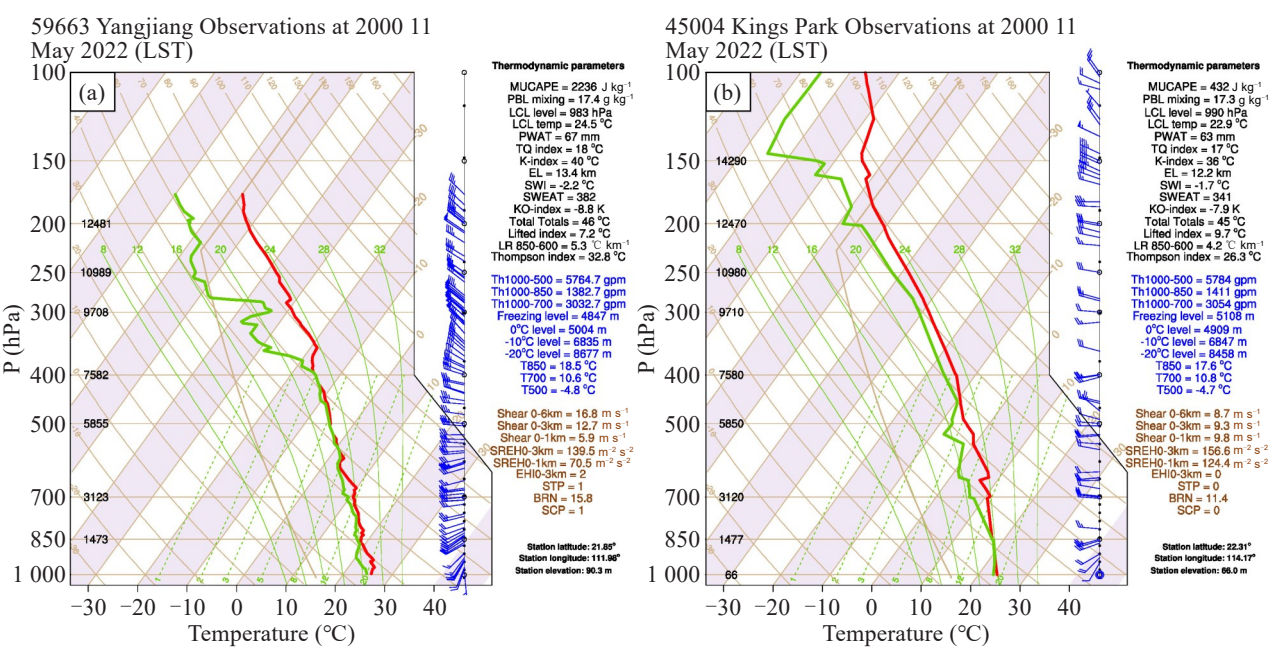

Figure 7. The skew T-lnP diagram and vertical wind profile (wind barbs, a full barb is 4 m s^{-1}) of (a) Yangjiang and (b) the Kings Park in Hong Kong sounding stations at 2000 LST 11 May. The red and green lines are the temperature and dew point temperature profiles, respectively.

The evolution of BLJ and SLLJ can be better observed from the data collected by AWSs and wind profile radar around the study area (Fig. 1a; Figs. 8-9). Two upstream AWSs located outside the study area showed that during the S1, the average wind speed at Nanpeng Island (59674, Fig. 8a) increased from less than 4 m s^{-1} to 8.1 m s^{-1} (at 0500 LST) from 0100 to 0500 LST, and the wind direction remained southwesterly. About 100 km downstream, the wind increased two hours later at Shan Tsui Pier (G2122, Fig. 8b) and continued to increase from 0300 to 0600 LST. Similar to the station of Nanpeng Island, the average wind speed increased from 3.8 m s^{-1} (0300 LST) to 7.6 m s^{-1} (0400 LST), and the wind direction changed from westerly to southwesterly. Within S2, the wind of the two AWSs increased again, reaching the standard of the BLJ (10 m s^{-1}) since 0600 LST. The maximum hourly average wind speed of station Nanpeng Island was 11.8 m s^{-1} (Fig. 8a), while the wind remained above 8 m s^{-1} at station Shan Tsui Pier from 0700 to 1700 LST, with a peak of 14.2 m s^{-1} at 1300 LST (Fig. 8b). The onset time and duration of strong wind in these two AWSs were highly consistent with the intensive rainfall period and duration in the study area, indicating that the BLJ (especially near the surface layer) was closely related to the evolution of heavy rainfall in the study area.

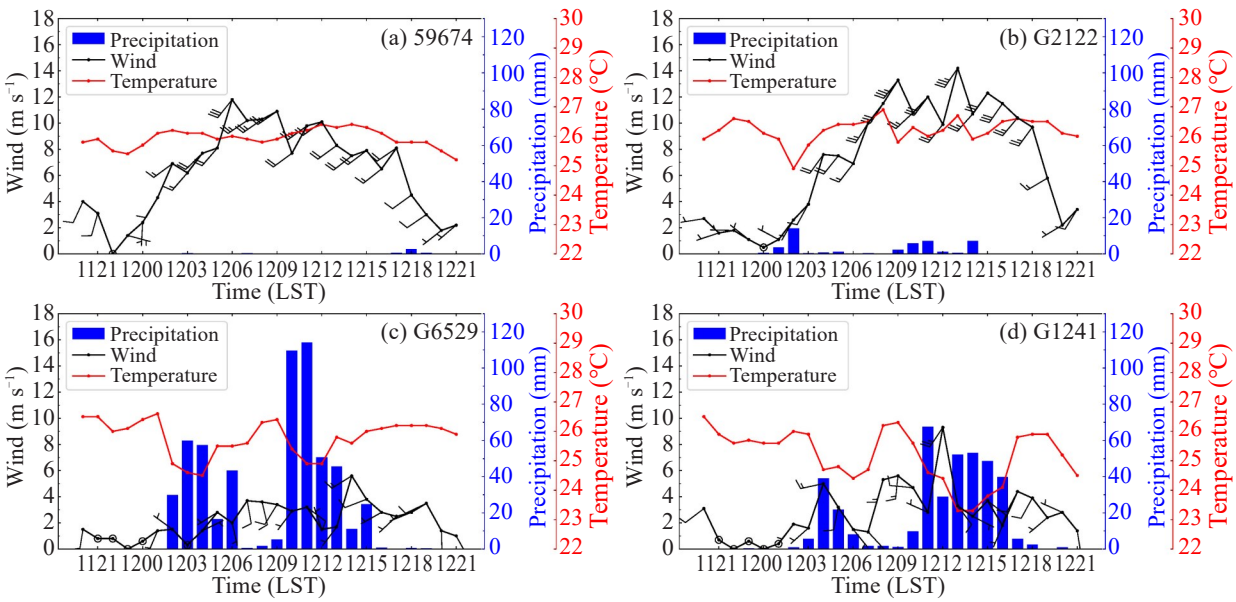

Figure 8. Hourly precipitation (blue bar, units: mm), temperature (red line, units: ℃), and average wind (barb, units: m s^{-1}; full barb represents 4 m s^{-1}). (a) 59674; (b) G2122; (c) G6529; (d) G1241.

In S1, a BLJ was observed near the ground at Hailing Island from 0000 to 0400 LST with a height of 0.2 km and shallow thickness of about 0.1−0.2 km, which lasted for about 4 hours. Meanwhile, the jets with more noticeable thickness appeared at a height above 1.5 km, corresponding to the SLLJ (Fig. 9a). At this stage, the location of a Zhuhai wind profile radar (located at the same position as station Pingsha, G1241) also experienced a short period of heavy rain (Fig. 8d). Both stations showed the same southwesterly to southerly winds, but the low-level wind speed below 0.5 km in Zhuhai was not greater than that in Hailing Island, even though the wind speed had strengthened for a while around 0100 to 0200 LST, which indicated that there was a convergence of wind speeds between the two stations (where the study area was located).

In S2, the wind speed in the two wind profile radars increased significantly from 0500 to 0800 LST, with the height of the jet stream center decreasing significantly and the strong wind area gradually dropping to lower than 1 km near the ground. From 0800 to 1100 LST, the thickness of the BLJ that appeared at about 0.2 km above Hailing Island Station was much shallower than that above station Zhuhai, and so the vertical range of SLLJ above station Hailing Island (Fig. 9a, 9b). At Hailing Island, the wind speed between the high and low-altitude jets was relatively weak, and the wind decreased with increasing height within the altitude of 1.5 km. The vertical distribution of the difference in wind speed caused convergence from lower to higher layers.

From 0500 to 0700 LST, the wind direction changed from southwesterly to westerly below 1 km over station Hailing Island. The wind speed increased significantly, resulting in warm and moist air being forced to lift over the coastal terrain, triggering the initial convection (Fig. 2d and 2e). At station Zhuhai, the wind direction below 1 km turned southerly from 0700 to 1000 LST (Fig. 9b), and there was obvious convergence of wind direction between upstream and downstream locations considering the winds at station Hailing Island. Moreover, the wind speed increased with increasing height at station Zhuhai within the boundary layer, and the airflow diverged from the lower layer to

the upper layer while it was inverse at station Hailing Island. The upstream and downstream effects influenced the westerly compensation flow, which was more conducive to the strengthening of the BLJ and the transport of more water vapor and energy from upstream to the study area, resulting in a significant increase in precipitation.

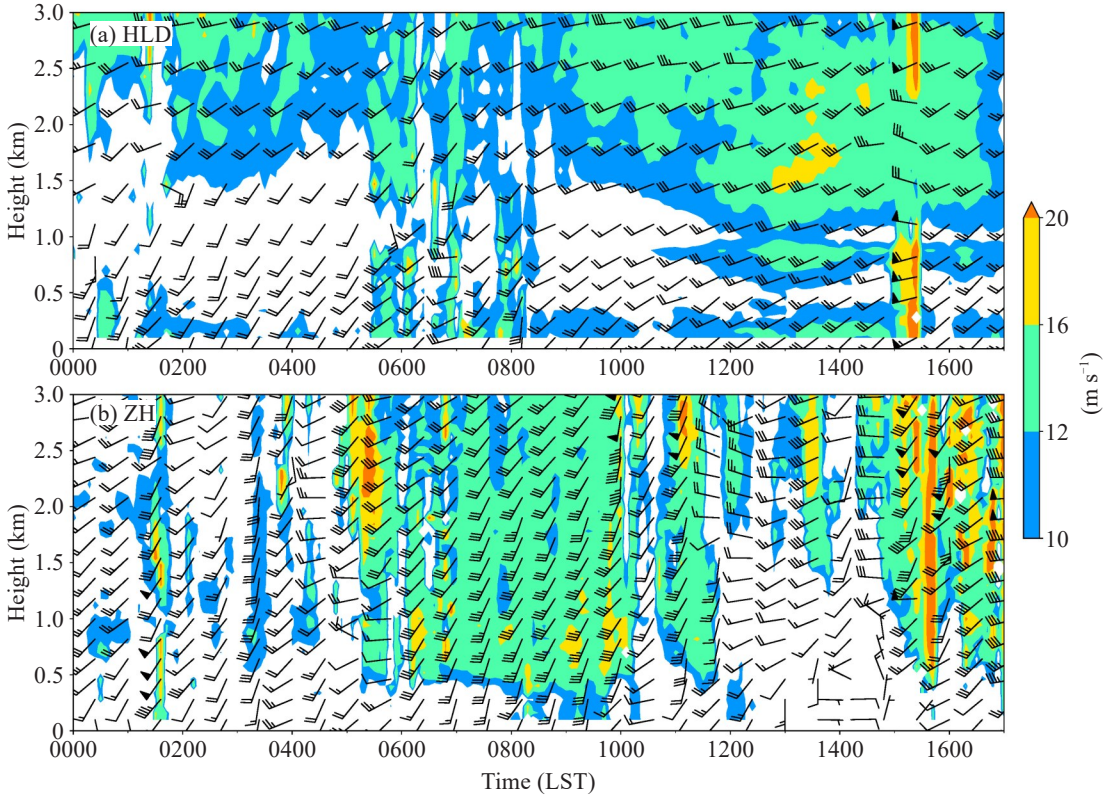

Figure 9. Observations from the wind profile radar from 0000 to 1700 LST 12 May 2022: (a) HLD wind profile radar; (b) ZH wind profile radar (shaded, wind speed, units: m s^{-1}; full barb represents 4 m s^{-1}, flag barb represents 20 m s^{-1}).

5 SURFACE MESOSCALE FEATURES

The two stages of heavy rainfall are not related to the LLJs only. To further explore the differences in triggering and maintenance mechanisms of precipitation processes in these two stages, the surface mesoscale characteristics are analyzed in this section. Fig. 10 shows the hourly rainfall, 2-m air temperature, and hourly winds recorded by the AWSs. At the beginning of S1 (at 0200 LST), a southwest warm and moist air flow moved northeast along the coastline, and the temperature difference between the upper and lower reaches of the study area was about 1 ℃ (Fig. 10a). Under the influence of coastal terrain, small-scale cyclonic circulation was formed in the piedmont (in front of Mt. LIM, Fig. 1a), and the near-surface convergence and uplift were generated (Fig. 11a). From 0200 to 0400 LST, with the continuous enhancement of the southwest warm and moist air flow (Fig. 8b), coastal convection was constantly triggered along the windward slope of Mt. LMD, Chixi. The convective cells then moved eastward, and the surface temperature in the study area dropped by 2 ℃ at 0400 LST due to the heavy rainfall (Fig. 10b). At the same time, a east-west-oriented mesoscale convergence line (MCL) was formed in the south of the convective area. The temperature difference between the north and south of the convergence line increased significantly (about 2−3 ℃). The joint influence of the BLJ enhancement and topographic uplift resulted in heavy precipitation with hourly rainfall exceeding 50 mm. Meanwhile, the mesoscale outflow boundary (MOB, blue lines in Fig. 10) appeared on the ground in the same movement direction as the convective cloud (Fig. 10b). The southwest warm and moist air was superimposed with the westerly wind produced by the MOB, which made the convective clouds move eastward rapidly. The near-surface convergence appeared in the convective cloud cluster (Fig. 11b), which was weaker and smaller in S1 than the convergence generated by the MOB in S2.

The southwest BLJ strengthened before the onset of S2 (0700 LST), and the average wind speed at the coastal AWSs exceeded 10 m s^{-1} (Fig. 8a, 8b; station 59674 and G2122). The southwest air flowed over Mt. NST to the north and confronted with the inland cooler air mass (the temperature difference between the sea and land was about 3 ℃), triggering convection. A southwest-northeast-oriented MCL (purple line in Fig.

10d) appeared in the middle of Jiangmen, and the reflectivity reached more than 35 dBZ (Fig 2d, 2e), resulting in heavy precipitation with hourly rainfall of more than 30 mm. From 0700 to 1000 LST, the wind direction in the study area turned southerly, and the mesoscale convective systems (MCSs) moved eastward and southward (Fig. 10d, 10e, 10f). The BLJ continued to enhance and converge on the upwind slope of Mt. LDM in Chixi (Fig. 11c, 11d). Under the influence of solar heating during the daytime, the air temperature inland rose rapidly (more significantly in the upstream region). From 0900 to 1000 LST, heavy rainfall reduced the near-surface temperature by about 2 ℃. The MOB became clearer at 1000 LST (Fig. 10f). When the MCSs moved southeast, the surface northwesterly wind converged with the ambient southwest warm and moist flow again, forming a strong convergence zone in front of convection motion (Fig. 11d). The unstable and humid air transported by the BLJ from the South China Sea was continuously lifted, resulting in extreme rainfall.

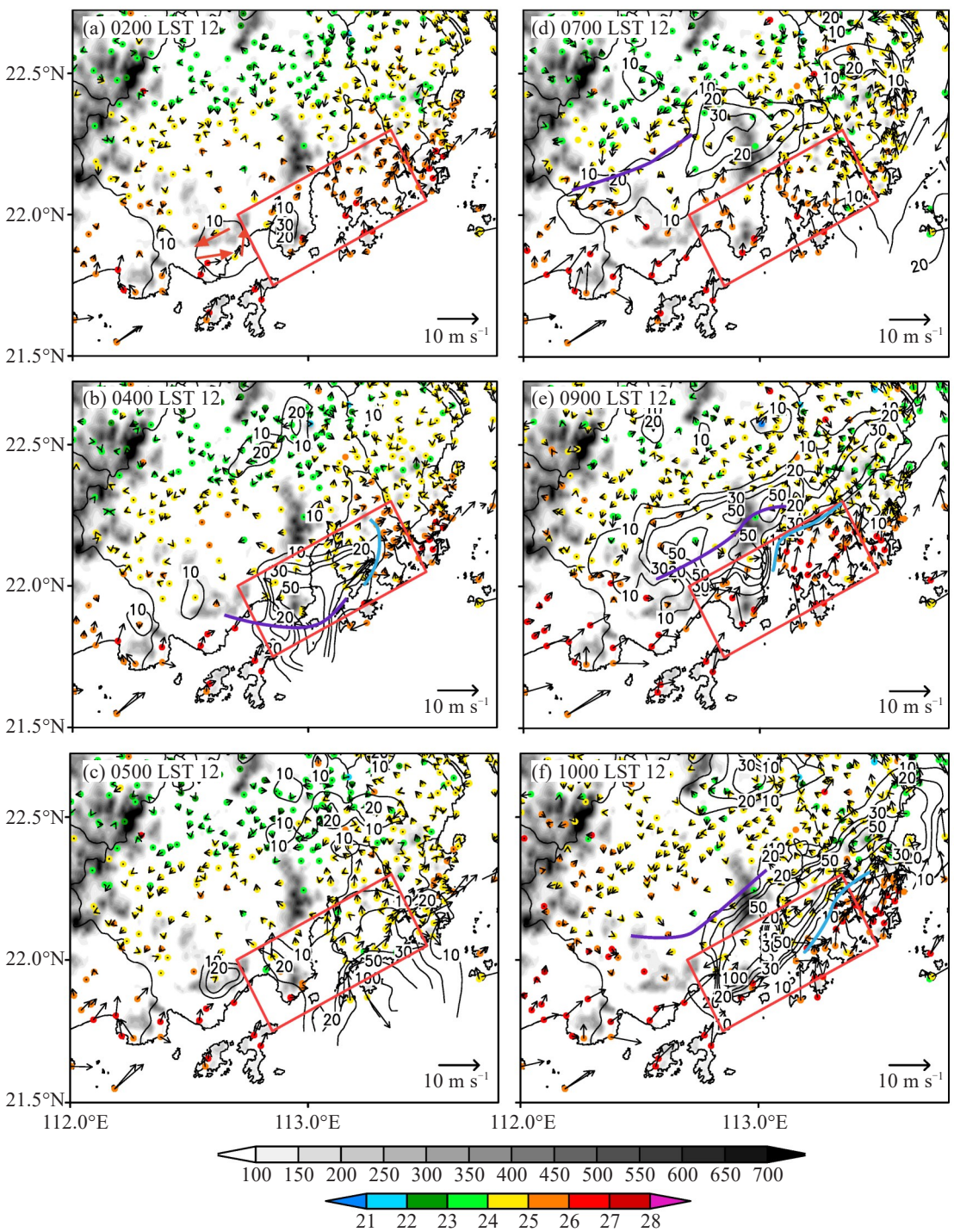

Figure 10. Temperature (shaded scatter, units: ℃), average hourly wind (vector, units: m s^{-1}), hourly precipitation (contour, units: mm) and altitude (shaded, units: m) (red arrow represents circulations; purple and blue line represents MCL and MOB, respectively).

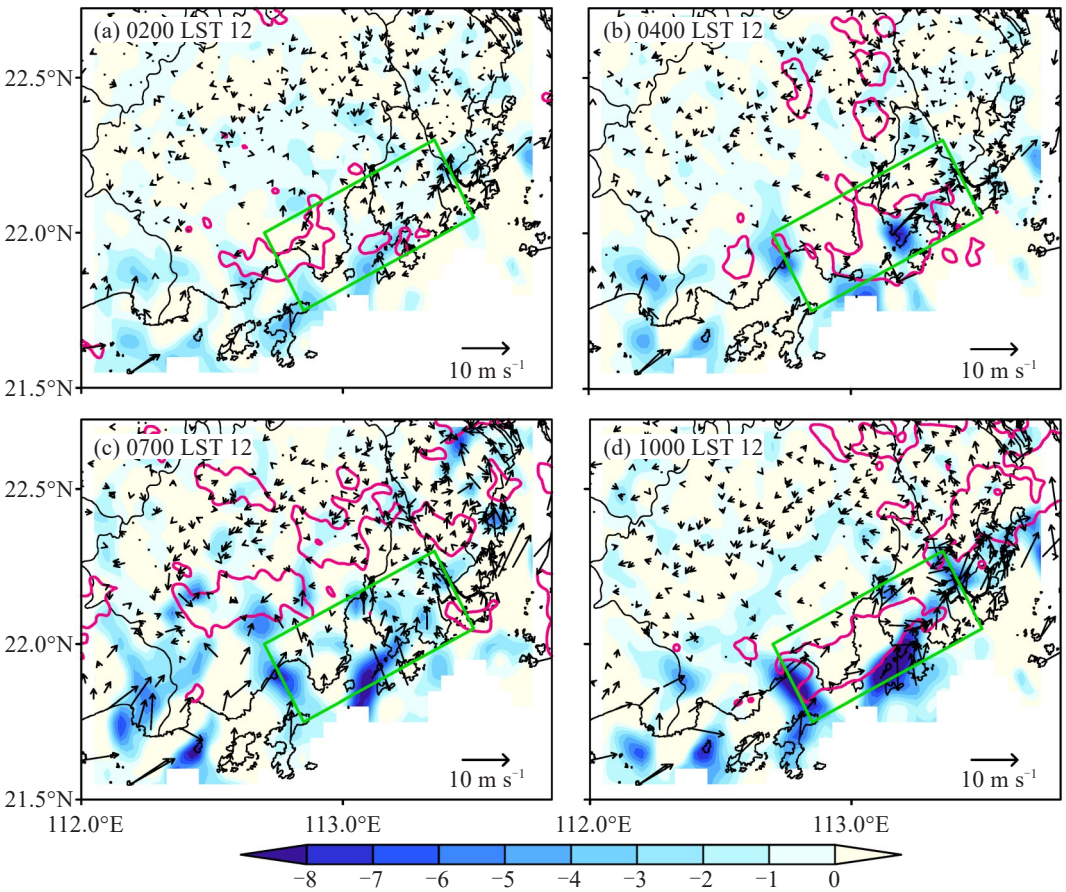

Figure 11. Hourly average wind (vector, units: m s^{-1}) and divergence field (shaded, units: 10^{-4} s^{-1}) at surface from AWSs (pink contour line represents radar reflectively CAPPI at height of 2 km ≥35 dBZ).

Overall, the prevailing wind direction near the surface was southwesterly from 0200 to 0500 LST in S1. After the enhancement of the southwest wind, topographic lifting was also enhanced, triggering strong convection that generated cold pools and a clear mesoscale outflow boundary (MOB). Moreover, the outflow boundary with the southwest wind superimposed with the ambient wind field accelerated the rainfall process and shortened the duration of heavy rain. The MOB on the surface had also been generated during the heavy rainfall from 0900 to 1400 LST in S2. However, the northwest-to-west wind from the outflow boundary converged with the ambient wind field (southerly wind) again, strengthening the rainfall and forming a positive feedback mechanism, making the convective system move slowly and maintaining the heavy rainfall.

6 MICROPHYSICAL CHARACTERISTICS OF RAINFALL

The above analysis shows that the heavy precipitation in S1 is mainly affected by the BLJ, while in S2, it is mainly due to the strengthened LLJs (including BLJ and SLLJ). The efficiency and duration of precipitation in S2 were stronger and longer than those in S1, respectively. This section will further explore the possible reasons for the similarities and differences in precipitation efficiency between the two stages in heavy rainfall under the influence of the LLJs from the perspective of microphysical characteristics.

Figure 12 presents the temporal evolution of polarimetric and lightning observations. Z_H, Z_{DR}, and K_{DP} represent the radar reflectivity factor, differential reflectivity factor, and specific differential phase, respectively. There is a gap at 0600 LST 12 May, separating S1 from S2. In the S1, the convection height was relatively high in the study area. The radar reflectivity of 40 dBZ extended to 9 km, exceeding the height of −20 ℃, and the large value center extended to the lower layer between the height of 1−5 km with time (Fig. 12a). The average development height of convective echo in 20 dBZ and 40 dBZ reached 20 km and 12 km, respectively (Fig. 12e). However, the Z_H in S2 showed characteristics of a lower mass center, and the vertical extension of strong echoes above 40 dBZ was wide. The lowest height of strong echoes in 40 dBZ extended to the ground and lasted 8 hours (0800 to 1600 LST) at 1 km, 2−3 times longer than in S1 (Fig. 12e). The K_{DP} value at the height of 1−3 km was greater than 1 deg km^{-1} during a short period from 0300 to 0400 LST in S1, indicating that the liquid water content increased sharply. The K_{DP} value below the height of 4 km during

0800 and 1300 LST in S2 was larger than that in S1, and it always remained above 1 deg km^{-1}, indicating that the lifting was strong and there was continuous water vapor being transported into the key area, resulting in large liquid water content at the lower layer (Fig. 12b). The Z_{DR} value was 0.8−1.0 dBZ below the height of 3 km from 0300 to 0400 LST in S1, while it exceeded 1.0 dBZ at the same height during 0800 to 0900 LST in S2 (Fig. 12c). It indicated that the particle size near the surface in S2 was larger than in S1, and the precipitation with large particle sizes lasted longer. In S1, the peak lightning frequency was less than 50 times, but the number of convective cells increased significantly, with the peak value approaching 10000 (Fig. 12d). The peak number of convective cells in S2 was about 1.5 times that in S1, and the lightning was more obvious, with a peak of 250 times, indicating more intense convection in S2. The values of K_{DP} and Z_{DR} below 3 km increased significantly in S2 (especially from 0800 to 0900 LST 12 May), which was probably influenced by the strengthening LLJs that intensified the collision and growth of raindrops in warm and moist conditions, increasing the liquid water content and the particle size of raindrops to a certain extent before falling to the ground. It was consistent with the evolution of precipitation in the AWSs. From 0800 to 0900 LST, raindrops collided, and the size increased, while the surface precipitation was not obvious, but from 0900 to 1000 LST, the short-time precipitation reached the peak of the whole heavy rainfall (Fig. 1e, 1f).

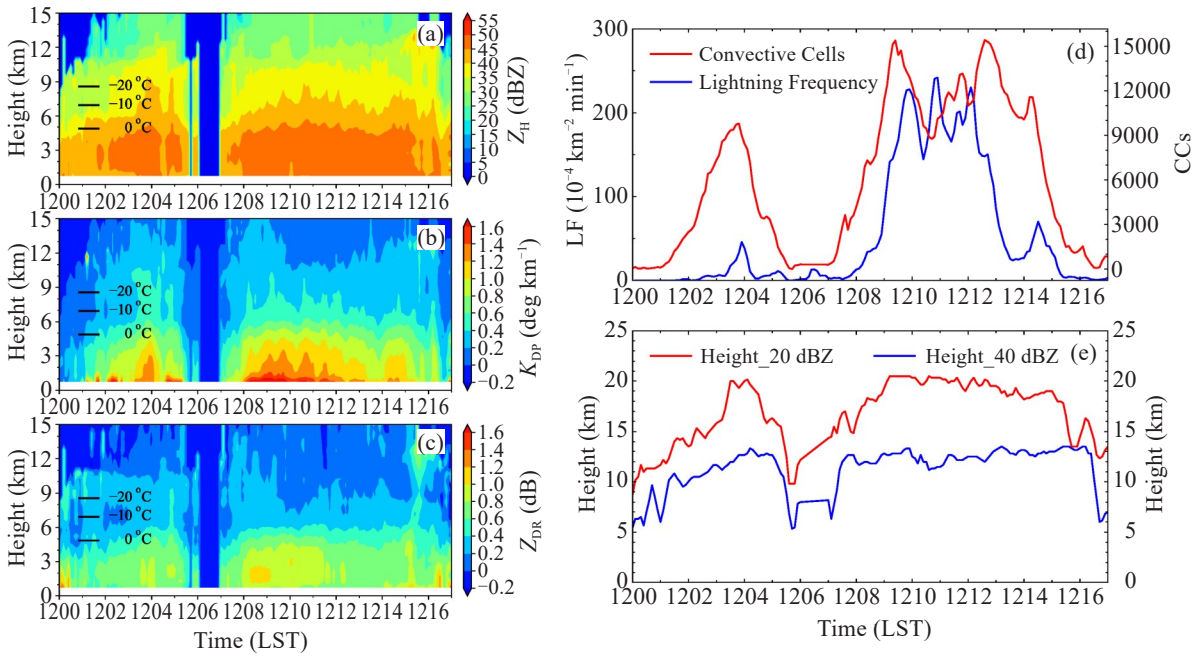

Figure 12. The time-height distributions of (a) Z_H (units: dBZ), (b) K_{DP} (units: deg km^{-1}), and (c) Z_{DR} (units: dB) averaged over the study area. The black lines represent levels −20 °C, −10 °C, and 0 °C from top to bottom, respectively. (d) Numbers of convective cells and lightning frequency (units: 10^{-4} km^{-2} min^{-1}). (e) Height map of convection echo over the study area. The blue line represents the level of 40 dBZ. The red line represents the level of 20 dBZ.

Below the 0 °C level, the high frequency center of Z_H in S2 was closer to 50 dBZ (Fig. 13a, 13b) than that in S1, and the mean value of Z_H in both stages increased first and then slightly decreased with the decrease of height (Fig. 13c). However, the average K_{DP} and Z_{DR} increased with decreasing height in the two stages, especially in S2 (Fig. 13f, 13i). This indicates that the collision and growth of raindrops under the warm cloud layer were more obvious in S2, and there were evaporation processes near the ground (0−3 km) in both stages.

The high frequency center of K_{DP} between levels 0 °C and −20 °C in S2 was wider (Fig. 13d, 13e). The mean value of K_{DP} in S2 was greater than 0 and larger than that in S1 (Fig. 13f). The frequency of Z_H value in S2 was greater than that in S1 at the same altitude (Fig. 13a, 13b). The corresponding Z_{DR} value at the high frequency center of Z_{DR} was also larger in S2 than in S1 (Fig. 13g, 13h). These results indicate that there were a large number of supercooled water droplets above the 0 °C level in S2, and the concentration of raindrops was high. Combined with the large proportion of WS and GR (Fig. 14d, 14e), the melting process of ice phase particles and the riming process in S2 were more significant.

From the altitude of −20 °C to 15 km, the mean Z_H in S2 was larger than in S1. The difference in the mean Z_H between these two stages increased with an increasing height between altitudes of 9−12 km (Fig. 13c). This may be due to the long duration of strong convection in S2, which increased the gap between the Z_H means in these two stages. This can also be

demonstrated in Fig. 12a. The K_{DP} in the two stages was relatively small, indicating that the liquid water content was low (Fig. 13f), and the aggregation of ice crystals in the S2 was more significant (by comparing the proportion of DS in Fig. 14d, 14e).

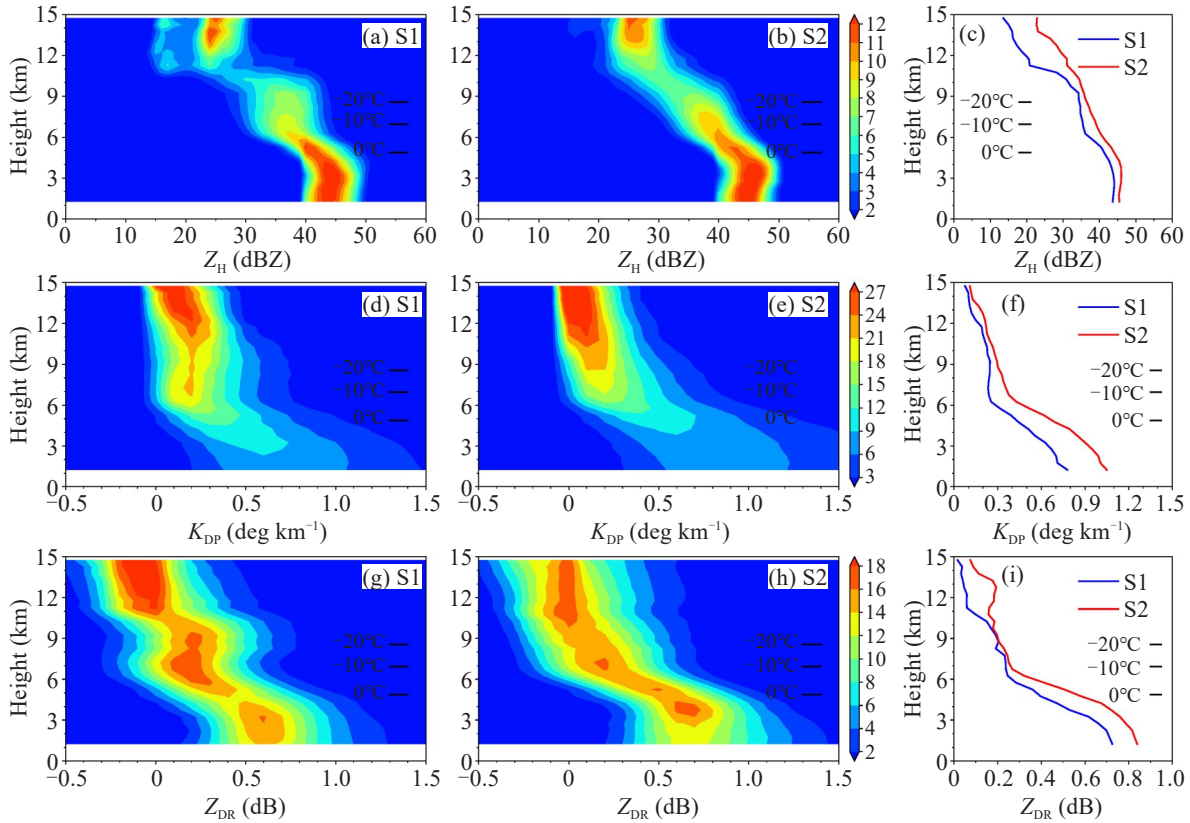

Figure 13. The contoured frequency by altitude diagrams (CFAD) from data over the study area (shaded, units: %). (a), (d), (g) are from stage 1, (b), (e), (h) are from stage 2, and (c), (f), (i) are percentile profiles that represent Z_H (units: dBZ), K_{DP} (units: deg km^{-1}) and Z_{DR} (units: dB) from top to bottom, respectively. The black lines represent levels −20 ℃, −10 ℃, and 0 ℃, respectively.

Based on the joint probability distribution functions (PDFs) of the mass-weighted mean diameter D_m and the normalized intercept $\log_{10}N_w$ (Fig. 14a, 14b), the concentrations of raindrops were high in both stages, which were comparable to those of the oceanic type and an order of magnitude higher than those of the continental type. The mean D_m was 1.61 mm in S2, 0.08 mm larger than that in S1, while the mean $\log_{10}N_w$ was 4.29 mm^{-1} m^{-3}, 0.02 mm^{-1} m^{-3} lower than that in S1, indicating that raindrops in S2 were larger and more conducive to heavy precipitation. Below the altitude of 3 km, Z_H decreased with the decreasing height, while K_{DP} increased in both S1 and S2 (Fig. 13c, 13f), indicating an obvious evaporation process at both stages (Liu et al. [84]; Ye et al. [85]). In the near-surface, the light and moderate rain (RA) occupied a smaller proportion in S2, with the average relative humidity of the AWSs in the study area decreasing (i.e., lower relative humidity in S2) and the wind speeds increasing (not shown), indicating that small raindrops in S2 evaporated more rapidly when falling to the surface, which made the average size of raindrops larger.

From the average vertical profile of LWC (liquid water content) and IWC (ice water content) (Fig. 14c), it showed a large LWC below the 0 ℃ isotherm, which was consistent with the larger K_{DP} in Fig. 12b. In S2, the maximum IWC and LWC over the study area were 1.0 and 3.2 g m^{-3}, which were 0.1 and 0.2 g m^{-3} larger than that in S1, respectively. Between the layer of 0 ℃ and −20 ℃, it produced more IWC in S2 than in S1, possibly because more cloud drops and raindrops were lifted above the melting layer with enhanced low-level convergence after the enhancement of the LLJs in S2, which was conducive to the riming process and the formation of graupel particles.

The Z_{DR} and K_{DP} in S2 were larger than in S1 within the layers of 0−10 ℃ (Fig. 13f, i), indicating that more supercooled water drops were formed in S2 and that graupel particles took up a significantly higher proportion than in S1 (Fig. 14d, 14e). Between the altitude of 2 km and the level of 0 ℃, the proportion of heavy rain (HR) and the mixture of rain and hail (RH) in S2 was higher than that in S1. Meanwhile, K_{DP} and Z_{DR} also increased significantly (Fig. 13f, 13i), indicating that with the increase in raindrop particle size and raindrop concentration, the melting process of graupel particles in S2 was more intense than that in S1. At ~1−2 km, RH accounted for about 50% in S2, and only 30%

in S1, indicating a significant difference between the two stages. Meanwhile, LWC also showed a great difference. Below 2 km, LWC in S2 increased with decreasing height, while it reversed in S1 (Fig. 13i). It indicated that the enhancement of the BLJ made the raindrops in the lower layer collide by merging and grow in size, resulting in the increase of LWC and the formation of raindrops with larger particle sizes near the surface.

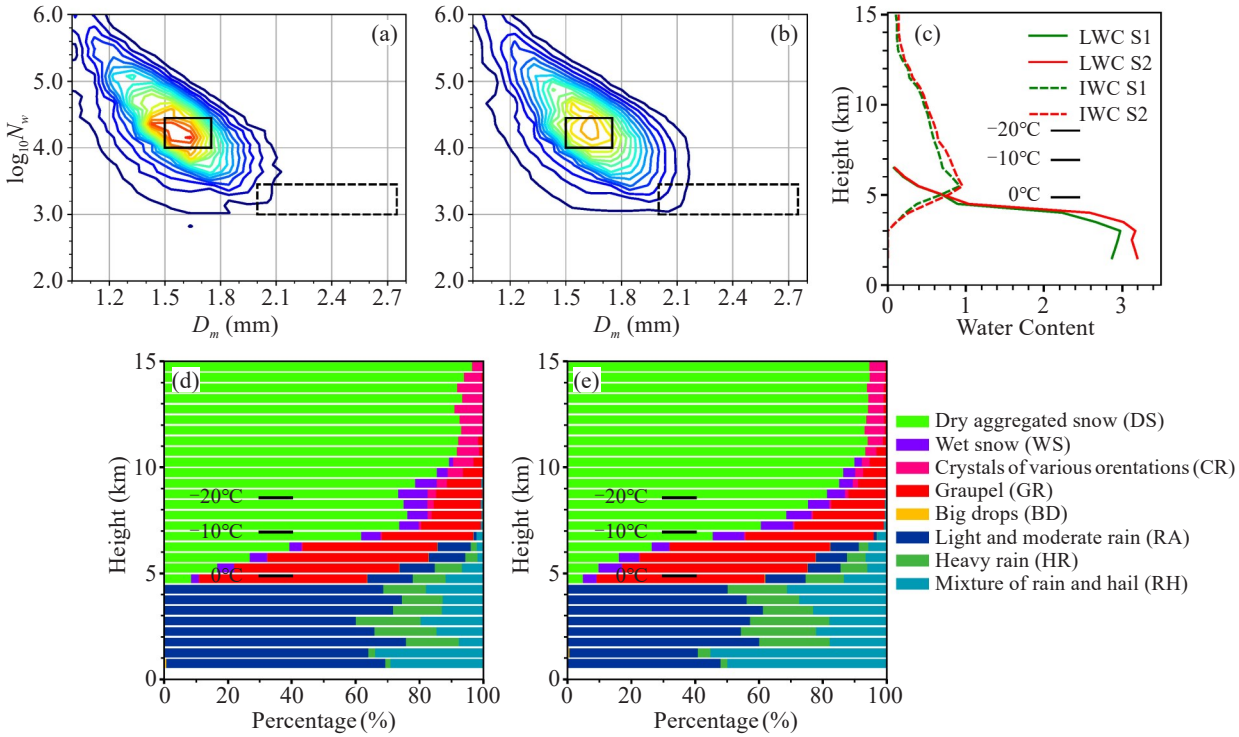

Figure 14. Frequency of D_m (units: mm) and $\log_{10}N_w$ (units: mm^{-1} m^{-3}) at an altitude of 2 km over the study area at the two stages of (a) S1 and (b) S2. The outermost line represents 5% contours, which ranges from 5% to 100% with an interval of 5%. The solid black box and the dotted box are the oceanic and continental convective areas proposed by Bringi and Chandrasekar[53]. (c) Vertical profiles of ice (dashed) and liquid (solid) water content (g m^{-3}) over the study area at the two stages. (d) Vertical distribution of the stacked frequency (%) of various hydrometeor types estimated by the HCA averaged for the study area in S1 and (e) S2, respectively. The short black lines represent the levels −20 °C, −10 °C, and 0 °C, respectively.

7 CONCLUSIONS

This study utilizes various observational data to investigate the thermodynamics and microphysical characteristics during two stages of a rainstorm process under the different influences of the LLJs (BLJ and SLLJ) over the south China Coast. The atmospheric thermal and dynamic conditions, mesoscale conditions, and microphysics characteristics are analyzed. The main conclusions are summarized as follows:

1. The heavy precipitation process influenced by the LLJs is divided into two stages: from 0000 to 0600 LST 12 May (S1) and from 0700 to 1700 LST 12 May (S2), respectively. In S1, the precipitation is mainly caused by the upper short-wave trough and the BLJ. In S2, the LLJs are greatly strengthened and move northward to affect the study area. The BLJ at 925 hPa and the SLLJ at 850 hPa form the coupling effect between high and low altitudes. The windward slope of the local topography plays an important role in extremely heavy precipitation. The altitudes of the oceanic warm and humid tongue dropped, and the advection transport is enhanced, strengthening the convergence on the study area near the surface (around the windward slope) and increasing the heavy rainfall duration. With the increasing vertical wind shear, higher moist baroclinity is conducive to developing vertical vorticity and maintaining rainstorms.

2. From S1 to S2, the altitudes of the upper divergence and jet stream centers decrease with time, and downward momentum transmission may exist. The LLJs strengthen, which is conducive to generating the secondary meridional circulation, thus promoting the thermal and dynamic exchange between high and low altitudes. Under the intensification of LLJs (in S2), convection is triggered upstream of the study area by terrain, converging from the lower layer to the upper layer in the upstream region and diverging in the downstream region within the boundary layer, forming the upstream and downstream wind speed compensation effect. Thus, the water vapor and energy from the upstream region are continuously transported downstream and accumulated under the influence of the terrain's windward slope, resulting in a significant

increase in precipitation over the study area.

3. MCL and MOB appear on the surface in both stages, and the temperature difference between MCL's north and south sides is large. The rise in inland temperature in S2 is more significant than in S1, and MOB exists longer. The outflow wind field of MOB is southwesterly in S1, consistent with the ambient wind field. Due to a smaller area of convergence that is left behind the MOB, the convection moves eastward quickly and causes a short duration of heavy rainfall in S1. In S2, the outflow wind field of MOB is northwesterly-westerly, which once again converges with the south wind of the environment, making the convection move more slowly and further enhance the convergence, forming a positive feedback mechanism. The positive feedback mechanism makes rainstorms maintain for a long time and more precipitation accumulate in S2.

4. In terms of microphysics, the mass center of strong echo in S1 is higher than in S2 but with shorter duration. The warm-rain process of the oceanic type characterizes both stages, but the convective intensity in S2 is significantly stronger than that in S1, featuring bigger drop sizes and lower concentrations. There are a lot of supercooled water drops and graupel particles above the 0℃ level in S2, and the ice phase (riming) process is stronger than in S1. At the same time, the K_{DP} and Z_{DR} values below level 0 ℃ in S2 are larger than in S1, suggesting that graupel particles melt and raindrops collide and grow significantly. Near the ground (below 3 km), the Z_H values in both stages decrease with decreasing height, but the K_{DP} and Z_{DR} values are opposite. The difference in K_{DP} value and Z_{DP} value in the two stages increases with decreasing height, and the K_{DP} value and Z_{DP} value are larger in S2, indicating that raindrops have obvious collision growth, larger particle size, higher LWC, and stronger evaporation in S2. In addition, LWC increases with decreasing height near the surface in S2, but it is the opposite in S1. Compared to S1, the lower relative humidity indicates that there are stronger evaporation and lower concentrations of small raindrop near the ground in S2, resulting in a larger proportion of HR and RH (large raindrops) and a lower proportion of RA near the ground in S2.

This study reveals the dynamic, thermal conditions and microphysical characteristics of an extremely heavy rain process along the south China coast under the influence of the LLJs using multi-source data, and the possible causes of the increase in precipitation are given. However, more cases are needed for the statistical study to further distinguish the microphysical differences of extremely heavy precipitation under the influence of the BLJ and SLLJ.

REFERENCES

[1] DING Y H. Monsoons over China [M]. Netherlands: Springer Dordrecht, 1994: 419, https://doi. org / 10.1007 / 978-94-015-8302-2

[2] DING Y H, CHAN J C. The East Asian summer monsoon: An overview [J]. Meteorology and Atmospheric Physics, 2005, 89: 117-142, https://doi. org / 10.1007 / s00703-005-0125-z

[3] LAU K M, YANG G J, SHEN S H. Seasonal and intraseasonal climatology of summer monsoon rainfall over East Asia [J]. Monthly Weather Review, 1988, 116(1): 18-37, https://doi.org/10.1175/1520-0493(1988)116<0018:SAICOS>2.0.CO;2

[4] LUO Y L, ZHANG R H, WAN Q L, et al. The Southern China Monsoon Rainfall Experiment (SCMREX) [J]. Bulletin of the American Meteorological Society, 2017, 98 (5): 999-1013, https://doi. org / 10.1175 / BAMS-D-15-00235.1

[5] LUO Y L, WANG H, ZHANG R H, et al. Comparison of rainfall characteristics and convective properties of monsoon precipitation systems over south China and the Yangtze and Huai River Basin [J]. Journal of Climate, 2013, 26(1): 110-132, https://doi.org/10.1175/JCLI-D-12-00100.1

[6] XIA R D, ZHANG D L, WANG B L. A 6-yr cloud-to-ground lightning climatology and its relationship to rainfall over central and eastern China [J]. Journal of Applied Meteorology and Climatology, 2015, 54(12): 2443-2460, https://doi.org/10.1175/JAMC-D-15-0029.1

[7] HUANG S S. Rain storm in south China in early summer [M]. Guangzhou: Guangdong Science and Technology Press, 1986(In Chinese).

[8] ZHAO S X, BEI N F, SUN J H. Mesoscale analysis of a heavy rainfall event over Hong Kong during a pre-rainy season in South China [J]. Advances in Atmospheric Sciences, 2007, 24: 555-572, https://doi. org / 10.1007 / s00376-007-0555-2

[9] LUO Y L. Advances in understanding the early-summer heavy rainfall over south China: Research and Forecast [C]// CHANG C P, LAU N G, JOHNSON R H, et al (eds), World Scientific Series on Asia-Pacific Weather and Climate, 2017: 215-226.

[10] DU Y, CHEN G X. Heavy rainfall associated with double low-level jets over southern China. Part I: Ensemble-based analysis [J]. Monthly Weather Review, 2018, 146 (11): 3827-3844, https://doi. org / 10.1175 / MWR-D-18-0101.1

[11] LIN L X, FENG Y R, HUANG Z. Technical guidance on weather forecasting in Guangdong Province [M]. Beijing: China Meteorological Press, 2006: 143-152 (in Chinese).

[12] CHEN G X, SHA W M, IWASAKI T. Diurnal variation of precipitation over southeastern China: Spatial distribution and its seasonality [J]. Journal of Geophysical Research: Atmospheres, 2009, 114(D13): 103, https://doi. org / 10.1029/2008JD011103

[13] CHEN X C, ZHAO K, XUE M. Spatial and temporal characteristics of warm season convection over Pearl River Delta region, China, based on 3 years of operational radar data [J]. Journal of Geophysical Research: Atmospheres, 2014, 119(22): 12447-12465, https://doi.org/10.1002/2014JD021965

[14] CHEN X C, ZHAO K, XUE M, et al. Radar-observed diurnal cycle and propagation of convection over the Pearl River delta during Mei-Yu season [J]. Journal of Geophysical Research: Atmospheres, 2015, 120(24):

12557-12575, https://doi.org/10.1002/2015JD023872
[15] HE L F, CHEN T, KONG Q. A review of studies on prefrontal torrential rain in South China [J]. Journal of Applied Meteorology Science, 2016, 27(5): 559-569 (in Chinese), https://doi.org/10.11898/1001-7313.20160505
[16] XIA R D, ZHAO S X. Diagnosis and modeling of Meso-β-scale systems of heavy rainfall in the warm sector ahead of the front in south China (middle part of Guangdong Province) in June 2005 [J]. Chinese Journal of Atmospheric Sciences, 2009, 33(3): 468-488(in Chinese), https://doi.org/10.3878/j.issn.1006-9895.2009.03.06
[17] LI B, LIU L P, ZHAO S X, et al. Numerical experiment of the effect of local low terrain on heavy rainstorm of south China [J]. Plateau Meteorology, 2013, 32(6): 1638-1650 (in Chinese), https://doi. org / 10.7522 / j. issn. 1000-0534.2012.00156
[18] WANG H, LUO Y L, JOU B J. Initiation, maintenance, and properties of convection in an extreme rainfall event during SCMREX: Observational analysis [J]. Journal of Geophysical Research: Atmospheres, 2014, 119(23): 13206-13232, https://doi.org/10.1002/2014JD022339
[19] RAO X N, ZHAO K, CHEN X C, et al. Roles of multi-scale orography in triggering nocturnal convection at a summer rainfall hotspot over the South China Coast: A case study [J]. Journal of Geophysical Research: Atmospheres, 2022, 127(12): e2022JD036503, https://doi.org/10.1029/2022JD036503
[20] WU N G, DING X, WEN Z P, et al. Contrasting frontal and warm-sector heavy rainfalls over South China during the early-summer rainy season [J]. Atmospheric Research, 2020, 235: 104693, https://doi. org / 10.1016 / j. atmosres.2019.104693
[21] LI H Q, HUANG Y J, HU S, et al. Roles of terrain, surface roughness, and cold pool outflows in an extreme rainfall even over the coastal region of South China [J]. Journal of Geophysical Research: Atmospheres, 2021, 126: e2021JD035556, https://doi. org / 10.1029 / 2021JD035556
[22] CHEN T J. Mesoscale features observed in the Chinese Taiwan Mei-Yu season [J]. Journal of the Meteorological Society of Japan, 1992, 70(1): 497-561, https://doi. org/10.2151/jmsj1965.70.1B_497
[23] XU W X, ZIPSER E, CHEN Y L, et al. An orography-associated extreme rainfall event during TiMREX: Initiation, storm evolution, and maintenance [J]. Monthly Weather Review, 2012, 140(8): 2555-2574, https://doi.org/10.1175/MWR-D-11-00208.1
[24] WU M W, LUO Y L. Mesoscale observational analysis of lifting mechanism of a warm-sector convective system producing the maximal daily precipitation in China mainland during the pre-summer rainy season of 2015 [J]. Journal of Meteorological Research, 2016, 30: 719-736, https://doi.org/10.1007/s13351-016-6089-8
[25] LIU X, LUO Y L, GUAN Z Y, et al. An extreme rainfall event in coastal south China during SCMREX-2014: Formation and roles of rainband and echo training [J]. Journal of Geophysical Research: Atmospheres, 2018, 123 (17): 9256-9278, https://doi.org/10.1029/2018JD028418
[26] WANG Q W, ZHANG Y, ZHU K F, et al. A case study of the initiation of parallel convective lines back - building from the south side of a mei-yu front over complex terrain [J]. Advances in Atmospheric Sciences, 2021, 38: 717-736, https://doi.org/10.1007/s00376-020-0216-2
[27] DU Y, ZHANG Q H, YING Y, et al. Characteristics of low - level jets in Shanghai during the 2008-2009 warm seasons as inferred from wind profiler radar data [J]. Journal of the Meteorological Society of Japan. Ser. II, 2012, 90(6): 891-903, https://doi. org / 10.2151 / jmsj. 2012-603
[28] DU Y, ZHANG Q H, CHEN Y L, et al. Numerical simulations of spatial distributions and diurnal variations of low-level jets in China during early summer [J]. Journal of Climate, 2014, 27(15): 5747-5767, https://doi.org/10.1175/JCLI-D-13-00571.1
[29] DU Y, CHEN Y L, ZHANG Q H. Numerical simulations of the boundary layer jet off the southeastern coast of China [J]. Monthly Weather Review, 2015, 143(4): 1212-1231, https://doi.org/10.1175/MWR-D-14-00348.1
[30] DU Y, ROTUNNO R, ZHANG Q H. Analysis of WRF simulated diurnal boundary layer winds in eastern China using a simple 1D model [J]. Journal of Atmospheric Sciences, 2015, 72(2): 714-727, https://doi. org / 10.1175 / JAS-D-14-0186.1
[31] ZHANG F, ZHANG Q H, DU Y, et al. Characteristics of coastal low-level jets in the Bohai Sea, China, during the early warm season [J]. Journal of Geophysical Research: Atmospheres, 2018, 123(24): 13763-13774, https://doi.org/10.1029/2018jd029242
[32] LI D L, STORCH H V, YIN B S, et al. Low-level jets over the Bohai Sea and Yellow Sea: Climatology, variability, and the relationship with regional atmospheric circulations [J]. Journal of Geophysical Research: Atmospheres, 2018, 123(10): 5240-5260, https://doi. org / 10.1029/2017JD027949
[33] SHU Z R, LI Q S, HE Y C, et al. Investigation of low-level jet characteristics based on wind profiler observations [J]. Journal of Wind Engineering and Industrial Aerodynamics, 2018, 174: 369-381, https://doi.org/10.1016/j.jweia.2018.01.035
[34] MIAO Y C, GUO J P, LIU S H, et al. The climatology of low - level jet in Beijing and Guangzhou, China [J]. Journal of Geophysical Research: Atmosphere, 2018, 123 (5): 2816-2830, https://doi.org/10.1002/2017JD027321
[35] STENSRUD D J. Importance of low-level jets to climate: A review [J]. Journal of Climate, 1996, 9(8): 1698-1711, https://doi. org / 10.1175 / 1520-0442(1996)009<1698: IOLLJT>2.0.CO;2
[36] RIFE D L, PINTO J O, MONAGHAN A J, et al. Global distribution and characteristics of diurnally varying low-level jets [J]. Journal of Climate, 2010, 23(19): 5041-5064, https://doi.org/10.1175/2010JCLI3514.1
[37] CHEN Y L, CHEN X A, ZHANG Y X. A diagnostic study of the low-level jet during TAMEX IOP 5 [J]. Monthly Weather Review, 1994, 122(10): 2257-2284, https://doi. org / 10.1175 / 1520-0493(1994)122<2257: ADSOTL>2.0.CO;2
[38] BLACKADAR A K. Boundary layer wind maxima and their significance for the growth of nocturnal inversions [J]. Bulletin of the American Meteorological Society, 1957, 38(5): 283-290, https://doi.org/10.1175/1520-0477-38.5.283
[39] HOLTON J R. The diurnal boundary layer wind oscillation above sloping terrain [J]. Tellus A: Dynamic Meteorology and Oceanography, 1967, 19(2): 199-205,

https://doi.org/10.3402/tellusa.v19i2.9766
[40] DU Y, ROTUNNO R. A simple analytical model of the nocturnal low-level jet over the Great Plains of the United States [J]. Journal of the Atmospheric Sciences, 2014, 71 (10): 3674-3683, https://doi. org / 10.1175 / JAS-D-14-0060.1
[41] SHAPIRO A, FEDOROVICH E, RAHIMI S. A unified theory for the Great Plains nocturnal low-level jet [J]. Journal of the Atmospheric Sciences, 2016, 73(8): 3037-3057, https://doi.org/10.1175/JAS-D-15-0307.1
[42] CHEN G T, YU C C. Study of low-level jet and extremely heavy rainfall over northern Taiwan, China in the mei-yu season [J]. Monthly Weather Review, 1988, 116(4): 884-891, https://doi.org/10.1175/1520-0493(1988)116<0884:SOLLJA>2.0.CO;2
[43] TAO S Y, CHEN L X. A review of recent research on the East Asian summer monsoon in China [M]// CHANG C P, KRISHNAMURTI T N (eds), Monsoon Meteorology. New York: Oxford University Press, 1987: 60-92.
[44] XUE M, LUO X, ZHU K F, et al. The controlling role of boundary layer inertial oscillations in meiyu frontal precipitation and its diurnal cycles over China [J]. Journal of Geophysical Research: Atmosphere, 2018, 123(10): 5090-5115, https://doi.org/10.1029/2018JD028368
[45] ASTLING E G, PAEGLE J, MILLER E, et al. Boundary layer control of nocturnal convection associated with a synoptic scale system [J]. Monthly Weather Review, 1985, 113(4): 540-552, https://doi.org/10.1175/1520-0493(1985)113<0540:BLCONC>2.0.CO;2
[46] TRIER S B, PARSONS D B. Evolution of environmental conditions preceding the development of a nocturnal mesoscale convective complex [J]. Monthly Weather Review, 1993, 121(4): 1078-1098, https://doi.org/10.1175/1520-0493(1993)121<1078:EOECPT>2.0.CO;2
[47] HIGGINS R W, YAO Y, YAROSH E S, et al. Influence of the Great Plains low-level jet on summertime precipitation and moisture transport over the central United States [J]. Journal of Climate, 1997, 10(3): 481-507, https://doi. org / 10.1175 / 1520-0442(1997)010<0481:IOTGPL>2.0.CO;2
[48] TRIER S B, DAVIS C A, AHIJEVYCH D A, et al. Mechanisms supporting long-lived episodes of propagating nocturnal convection within a 7-day WRF model simulation [J]. Journal of the Atmospheric Sciences, 2006, 63(10): 2437-2461, https://doi. org / 10.1175/JAS3768.1
[49] CHEN G, ZHAO K, ZHANG G F, et al. Improving polarimetric C-band radar rainfall estimation with two-dimensional video disdrometer observations in eastern China [J]. Journal of Hydrometeorology, 2017, 18(5): 1375-1391, https://doi.org/10.1175/JHM-D-16-0215.1
[50] DU Y, CHENG G X. Climatology of low-level jets and their impact on rainfall over southern China during the early-summer rainy season [J]. Journal of Climate, 2019, 32(24): 8813-8833, https://doi. org / 10.1175 / JCLI-D-19-0306.1
[51] BRINGI V N, CHANDRASEKAR V, HUBBERT J, et al. Raindrop size distribution in different climatic regimes from disdrometer and dual-polarized Radar analysis [J]. Journal of the Atmospheric Sciences, 2003, 60(2): 354-365, https://doi. org / 10.1175 / 1520-0469(2003)060<0354:RSDIDC>2.0.CO;2
[52] KUMJIAN M R, RYZHKOV A V. Polarimetric signatures in supercell thunderstorms [J]. Journal of Applied Meteorology and Climatology, 2008, 47(7): 1940-1961, https://doi.org/10.1175/2007JAMC1874.1
[53] BRINGI V N, CHANDRASEKAR V. Polarimetric Doppler weather radar: Principles and applications [M]. U.K.: Cambridge University Press, 2001: 636.
[54] ZRNIC D S, RYZHKOV A V. Polarimetry for weather surveillance radars [J]. Bulletin of the American Meteorological Society, 1999, 80(3): 389-406, https://doi.org/10.1175/1520-0477(1999)080<0389:pfwsr>2.0.co;2
[55] BARNES H C, HOUZE Jr R A. Precipitation hydrometeor type relative to the mesoscale airflow in mature oceanic deep convection of the Madden-Julian oscillation [J]. Journal of Geophysical Research: Atmospheres, 2014, 119(24): 13990-14014, https://doi.org/10.1002/2014jd022241
[56] CHEN G, ZHAO K, WEN L, et al. Microphysical characteristics of three convective events with intense rainfall observed by polarimetric radar and disdrometer in Eastern China [J]. Remote Sensing, 2019, 11(17): 2004, https://doi.org/10.3390/rs11172004
[57] LANG T J, RUTLEDGE S A, CIFELLI R. Polarimetric radar observations of convection in northwestern Mexico during the North American Monsoon Experiment [J]. Journal of Hydrometeorology, 11(6): 1345-1357, https://doi.org/10.1175/2010jhm1247.1
[58] MATSUI T, DOLAN B, LGUCHI T, et al. Polarimetric radar characteristics of simulated and observed intense convective cores for a midlatitude continental and tropical maritime environment [J]. Journal of Hydrometeorology, 2020, 21(3): 501-517, https://doi. org / 10.1175 / jhm-d-19-0185.1
[59] ROWE A K, RUTLEDGE S A, LANG T J. Investigation of microphysical processes occurring in isolated convection during NAME [J]. Monthly Weather Review, 2011, 139(2): 424-443, https://doi. org / 10.1175 / 2010mwr3494.1
[60] ROWE A K, RUTLEDGE S A, LANG T J. Investigation of microphysical processes occurring in organized convection during NAME [J]. Monthly Weather Review, 2012, 140(7): 2168-2187, https://doi.org/10.1175/mwr-d-11-00124.1
[61] WEN J, ZHAO K, HUANG H, et al. Evolution of microphysical structure of a subtropical squall line observed by a polarimetric radar and a disdrometer during OPACC in Eastern China [J]. Journal of Geophysical Research: Atmospheres, 2017, 122(15): 8033-8050, https://doi.org/10.1002/2016jd026346
[62] PU Y L, HU S, LUO Y L, et al. Multiscale Perspectives on an extreme warm-sector rainfall event over coastal south China [J]. Remote Sensing, 2022, 14(13): 3110, https://doi.org/10.3390/rs14133110
[63] LI H Q, WAN Q L, PENG D D, et al. Multiscale analysis of a record-breaking heavy rainfall event in Guangdong, China [J]. Atmospheric Research, 2020, 232: 104703, https://doi.org/10.1016/j.atmosres.2019.104703
[64] WU G X, CAI Y P, TANG X J. Moist potential vorticity and slantwise vorticity development [J]. Acta Meteorologica Sinica, 1995, 53(4): 387-405 (in Chinese), https://doi.org/ 10.11676/qxxb1995.045
[65] HOSKINS B J. The role of potential vorticity in

symmetric stability and instability [J]. Quarterly Journal of the Royal Meteorology Society, 1974, 100(425): 480-482, https://doi.org/10.1002/qj.49710042520

[66] HOSKINS, B J. On the use and significance of isentropic potential vorticity maps [J]. Quarterly Journal of the Royal Meteorology Society, 1985, 111(480): 877-964, https://doi.org/10.1002/qj.49711147002

[67] MENG W G, WANG A Y, LI J N, et al. Moist potential vorticity analysis of the heavy rainfall and mesoscale convective systems in south China [J]. Chinese Journal of Atmospheric Sciences, 2004, 28(3):330-341 (in Chinese), https://doi.org/ 10.3878/j.issn.1006-9895.2004.03.02.

[68] PARK H S, RYZHKOV A V, ZRNIC D S, et al. The hydrometeor classification algorithm for the polarimetric WSR-88D: Description and application to an MCS [J]. Weather and Forecasting, 2009, 24(3): 730-748, https://doi.org/10.1175/2008WAF2222205.1

[69] WU C, LIU L P, WEI M, et al. Statistics-based optimization of the polarimetric radar hydrometeor classification algorithm and its application for a squall line in south China [J]. Advances in Atmospheric Sciences, 2018, 35: 296-316, https://doi. org / 10.1007 / s00376-017-6241-0

[70] ZHANG G, VIVEKANANDAN J, BRANDES E. A method for estimating rain rate and drop size distribution from polarimetric radar measurements[J]. IEEE Transactions on Geoscience Remote Sensing, 2001, 39 (4): 830-841, https://doi.org/10.1109/36.917906

[71] GOLESTANI Y, CHANDRASEKAR V, BRINGI V N. Intercomparison of multiparameter radar measurements [C]// Preprints, 24th Conference on Radar Meteorology, Tallahassee., American Meteorology Society, 1989: 309-314.

[72] CIFELLI R, PETERSEN W A, CAREY L D, et al. Radar observations of the kinematic, microphysical, and precipitation characteristics of two MCSs in TRMM LBA [J]. Journal of Geophysical Research: Atmospheres, 2002, 107(D20): LBA 44-1-LBA 44-16, https://doi.org/10.1029/2000JD000264

[73] WANG J J, CAREY L D. The development and structure of an oceanic squall-line system during the South China Sea Monsoon Experiment [J]. Monthly Weather Review, 2005, 133(6): 1544-1561, https://doi. org / 10.1175 / mwr2933.1

[74] CHANG W Y, LEE W C, LIOU Y C. The kinematic and microphysical characteristics and associated precipitation efficiency of subtropical convection during SoWMEX / TiMREX [J]. Monthly Weather Review, 2015, 143(1): 317-340, https://doi.org/10.1175/MWR-D-14-00081.1

[75] CAREY L D, RUTLEDGE S A. The relationship between precipitation and lightning in tropical island convection: A C-band polarimetric radar study [J]. Monthly Weather Review, 2000, 128(8): 2687-2710, https://doi.org/10.1175/1520-0493(2000)128<2687:trbpal>2.0.co;2

[76] WANG M J, ZHAO K, XUE M, et al. Precipitation microphysics characteristics of a Typhoon Matmo (2014) rainband after landfall over eastern China based on polarimetric radar observations [J]. Journal of Geophysical Research: Atmospheres, 2016, 121(20): 12415-12433, https://doi.org/10.1002/2016JD025307

[77] WU D, ZHAO K, KUMJIAN M R, et al. Kinematics and microphysics of convection in the outer rainband of typhoon Nida (2016) revealed by polarimetric radar [J]. Monthly Weather Review, 2018, 146(7): 2147-2159, https://doi.org/10.1175/MWR-D-17-0320.1

[78] MARSHALL J S, PALMER W M. The distribution of raindrops with size [J]. Journal of the Atmospheric Sciences, 1948, 5(4): 165-166, https://doi. org / 10.1175 / 1520-0469(1948)005<0165:TDORWS>2.0.CO;2

[79] ZHANG G F, VIVEKANANDAN J, BRANDES E, et al. The shape-slope relation in observed Gamma raindrop size distributions: Statistical error or useful information? [J]. Journal of Atmospheric and Oceanic Technology, 2003, 20(8): 1106-1119, https://doi. org / 10.1175 / 1520-0426(2003)020<1106:tsriog>2.0.co;2

[80] WU Z J, BAO Y X, ZHU T, et al. Study on the mechanism of Low-Level Jet in a heavy rainfall in the Yangtze River Basin [J]. Journal of Tropical Meteorology, 2019, 35(3): 409-422 (in Chinese), https://doi. org / 10.16032/j.issn.1004-4965.2019.038

[81] JIN W, QU Y, YAO X P, et al. Mesoscale structure and evolution of the low-level jet and its relationship with the heavy rainfall during a torrential rain process [J]. Meteorological Monthly, 2007, 33(12): 31-38 (in Chinese), https://doi. org/ 10.7519 / j. issn. 1000-0526.2007.12.005.

[82] CAO C Y, JIANG Y, SUN X M. Relationship between low level jet stream and heavy precipitation in a heavy rainfall event [J]. Meteorological Monthly, 2006, 32(6): 102-106 (in Chinese), https://doi.org/10.7519/j.issn.1000-0526.2006.6.018.

[83] MARKOWSKI P, RICHARDSON Y. Mesoscale Meteorology in Midlatitudes [M]. Wiley-Blackwell: Oxford, UK, 2010: 430.

[84] LIU X T, RUAN Z, HU S, et al. The Longmen Cloud Physics Field Experiment Base, China Meteorological Administration [J]. Journal of Tropical Meteorology, 2023, 29(1): 1-20, https://doi. org / 10.46267 / j. 1006-8775.2023.001

[85] YE L M, LIU X T, PU Y L, et al. Contrasts in the evolution and microphysical features of two convective systems during a heavy rainfall event along the coast of south China [J]. Atmosphere, 2022, 13: 1549. https://doi.org/10.3390/atmos13101549

Citation: XU Bi-yu, LI Hui-qi, YE Lang-ming, et al. Thermodynamics and Microphysical Characteristics of an Extreme Rainfall Event under the Influence of a Low-level Jet over the South China Coast [J]. Journal of Tropical Meteorology, 2023, 29(2): 216-235, https://doi.org/10.46267/j.1006-8775.2023.017